FISFVIFR

Contents lists available at ScienceDirect

# **International Journal of Plasticity**

journal homepage: www.elsevier.com/locate/ijplas





# Deformation, dislocation evolution and the non-Schmid effect in body-centered-cubic single- and polycrystal tantalum

Seunghyeon Lee <sup>a</sup>, Hansohl Cho <sup>a,\*</sup>, Curt A. Bronkhorst <sup>b</sup>, Reeju Pokharel <sup>c</sup>, Donald W. Brown <sup>c</sup>, Bjørn Clausen <sup>c</sup>, Sven C. Vogel <sup>c</sup>, Veronica Anghel <sup>c</sup>, George T. Gray III <sup>c</sup>, Jason R. Mayeur <sup>d</sup>

- a Department of Aerospace Engineering, Korea Advanced Institute of Science and Technology, Daejeon, 34141, Republic of Korea
- <sup>b</sup> Department of Mechanical Engineering, University of Wisconsin, Madison, WI 53706, USA
- <sup>c</sup> Materials Science & Technology Division, Los Alamos National Laboratory, Los Alamos, NM 87545, USA
- <sup>d</sup> Oak Ridge National Laboratory, Oak Ridge, TN 37830, USA

#### ARTICLE INFO

# Keywords: Crystal plasticity Body-centered-cubic (bcc) crystals Single- and polycrystal tantalum Slip instability Non-Schmid effects ex situ neutron diffraction measurement Dislocation density evolution

#### ABSTRACT

A physically-informed continuum crystal plasticity model is presented to elucidate deformation mechanisms, dislocation evolution and the non-Schmid effect in body-centered-cubic (bcc) tantalum widely used as a key structural material for mechanical and thermal extremes. We show the unified structural modeling framework informed by mesoscopic dislocation dynamics simulations is capable of capturing salient features of the large inelastic behavior of tantalum at quasi-static (10<sup>-3</sup> s<sup>-1</sup>) to extreme strain rates (5000 s<sup>-1</sup>) and at low (77 K) to high temperatures (873 K) at both single- and polycrystal levels. We also present predictive capabilities of the model for microstructural evolution in the material. To this end, we investigate the effects of dislocation interactions on slip activities, instability and the non-Schmid behavior at the single crystal level. Furthermore, ex situ measurements on crystallographic texture evolution and dislocation density growth are carried out for polycrystal tantalum specimens at increasing strains. Numerical simulation results also support that the modeling framework is capable of capturing the main features of the polycrystal behavior over a wide range of strains, strain rates and temperatures. The theoretical, experimental and numerical results at both single- and polycrystal levels provide critical insight into the underlying physical pictures for micro- and macroscopic responses and their relations in this important class of refractory bcc materials undergoing large inelastic deformations.

#### 1. Introduction

Body-centered-cubic (bcc) crystalline tantalum is a refractory transition metal in the Group V. It has been widely used for key structural components often exposed to harsh physico-chemical environments due to its superb strength, ductility and corrosion and radiation resistance over a wide range of strains, strain rates and temperatures. The mechanical behavior of tantalum and its alloys has been a focal point of research to facilitate their applications in diverse mechanical, thermal and chemical extremes. Recently, these materials are also finding new avenues towards high performance metallic composites and laminates for biological, defense and energy applications (Pappu et al., 1996; Matsuno et al., 2001; Mayeur et al., 2013).

E-mail addresses: hansohl@kaist.ac.kr (H. Cho), cbronkhorst@wisc.edu (C.A. Bronkhorst).

<sup>\*</sup> Corresponding author.

Inelasticity in bcc materials has been a long-standing interest. Inelastic deformation mechanisms in bcc materials are fundamentally different from those in face-centered-cubic (fcc) or hexagonal materials. Inelastic slip in bcc materials is governed mainly by the motion of screw dislocations in a close-packed direction of  $\langle 111 \rangle$  on several possible different planes of  $\langle 110 \rangle$ ,  $\langle 112 \rangle$  or  $\langle 123 \rangle$ . As reviewed in Seeger (2001), Weinberger et al. (2013) and Lim et al. (2020), slip occurs predominantly on  $\langle 110 \rangle$  planes at low temperature. Slip on  $\langle 112 \rangle$  and  $\langle 123 \rangle$  planes is also observed at elevated temperatures. However, the transition mechanism between these slip modes have been deemed elusive in bcc crystals which will be further discussed in Section 2.3. Furthermore, inelastic slip of screw dislocations is a thermally-activated process over a wide range of strain rates and temperatures as well postulated in Stainier et al. (2002) and Nguyen et al. (2021). The high Peierls stress (or lattice friction) associated with screw dislocations and the thermally-activated formation of kink pairs give rise to strongly rate- and temperature-dependent inelastic features in bcc crystals and their alloys. Over the past several decades, the rate- and temperature-dependent inelasticity has been investigated for single crystalline tantalum (Stainier et al., 2002; Lim et al., 2020; Nguyen et al., 2021) and polycrystalline tantalum (Kothari and Anand, 1998; Nemat-Nasser et al., 1998).

In conjunction with the experimental and theoretical studies on the rate- and temperature-dependent inelastic features due to the complex motion of screw dislocations, the breakdown of the classical Schmid law also known as non-Schmid effects has been widely reported for bcc materials. A non-planar core structure of the dominant screw dislocations gives rise to such abnormal plasticity features as tension-compression asymmetry and orientation-dependent critical shear stress for the onset of inelastic slip as experimentally evidenced in Sherwood et al. (1967). Moreover, the underlying physics of the non-planar core structure in (111) screw dislocations has been studied via atomistic simulations (Gröger et al., 2008a,b; Gröger and Vitek, 2020; Gröger, 2021) and abinitio calculations (Bienvenu et al., 2022). Manifestation of non-Schmid effects has been well evidenced in experiments and atomistic simulations for tantalum materials, especially at low temperature (Sherwood et al., 1967; Holzer et al., 2021; Bienvenu et al., 2022).

Meanwhile, based upon the classical papers by Asaro and Needleman (1985), Kalidindi et al. (1992) and Cuitiño and Ortiz (1993), numerous single crystal plasticity models have been proposed and have found success in elucidating the key features in the mechanical behaviors of bcc single crystals including tantalum (Nguyen et al., 2021),  $\alpha$ -iron (Narayanan et al., 2014), niobium (Mayeur et al., 2013), tungsten (Cereceda et al., 2016) and their alloys (Ardeljan et al., 2014) under diverse loading scenarios over a wide range of crystallographic orientations. Moreover, as recently reviewed in Cho et al. (2018), continuum single crystal plasticity models have been extended to capture the non-Schmid behavior of tantalum and other bcc materials, especially at low temperatures, informed from atomistic simulations on the non-planar core structure of an isolated screw dislocation under diverse loading conditions (Gröger et al., 2008a,b).

There have been many efforts to accurately model the large inelastic behavior of polycrystalline bcc materials. Phenomenological isotropic elastic-plastic constitutive theories including mechanical threshold stress (MTS) model (Follansbee and Kocks, 1988) and Zerilli-Armstrong model (Zerilli and Armstrong, 1987) have found success in capturing the rate- and temperature dependent yield and hardening behaviors in bcc polycrystals (Chen and Gray, 1996; Lim et al., 2015, 2016). Although these isotropic constitutive models described the plastic deformation features reasonably well, they could not account for microstructural details involving texture and dislocation evolutions at the polycrystal levels. In tandem with the isotropic theories, the Taylor-type polycrystal models (Asaro and Needleman, 1985) based on the single crystal plasticity theories have found success in part in modeling the large inelastic behavior and the evolution of crystallographic textures during deformation in many fcc (Asaro and Needleman, 1985; Kalidindi et al., 1992) and bcc materials (Kothari and Anand, 1998; Nemat-Nasser et al., 1998). Polycrystal models have been recently extended to satisfy both equilibrium and geometric compatibility, for which each of the finite elements represents one single crystalline grain (Kalidindi et al., 1992; Bronkhorst et al., 1992; Anand, 2004). Furthermore, the recent progress in electron backscatter diffraction analysis of actual polycrystalline microstructures has enabled better modeling of the polycrystalline behavior with more realistic microstructures and networks of grains and grain boundaries especially for polycrystal bcc materials and laminates (Lim et al., 2014, 2018). However, in these papers on bcc polycrystals, the details regarding constituent single crystal behavior have not been presented independently of the polycrystal behavior; i.e., the previous modeling efforts have been focused mainly on the effective responses of the polycrystals. Furthermore, as the extreme thermomechanical responses associated with shear band localization, ductile damage and spallation upon harsh loading events have recently received great attention (Bronkhorst et al., 2016, 2021; Francis et al., 2021), there has been an increasing need for unified structural modeling framework for both bcc tantalum single- and polycrystals at a wide range of strains, strain rates and temperatures.

This work aims at elucidating deformation mechanisms and dislocation structure evolution in bcc single- and polycrystal tantalum using a suite of theoretical modeling, experimentation and numerical simulation. We present a physically-informed finite deformation single crystal viscoplasticity model in which the underlying physics of dislocation evolution and interaction throughout the slip systems is taken into account. Then, we show the predictive capabilities of the single crystal model at strain rates ranging from 0.001 s<sup>-1</sup> to 10<sup>3</sup> s<sup>-1</sup> and at temperatures ranging from 77 K to 873 K for various crystallographic orientations. We also show strong latent hardening, herein due to collinear interactions throughout slip systems evidenced in the recent dislocation dynamics simulations (Madec and Kubin, 2017), may give rise to slip instability and bifurcation in tantalum single crystals. Motivated by the instability analysis, we further extend the dislocation density-based single crystal model to accurately capture the non-Schmid effect, herein tension–compression asymmetry, experimentally evidenced in tantalum single crystals loaded especially in high symmetry orientations at low temperature. The model is then validated for the inelastic features in polycrystal tantalum. To this end, we conducted an extensive set of new experiments for polycrystal specimens including mechanical tests and *ex situ* neutron diffraction measurements on dislocation density growth and texture evolution, and compared the experimental data with the corresponding numerical simulation results. Using the unified modeling framework for both single- and polycrystal tantalum, we further develop critical insights into the inelastic deformation mechanisms at both microscopic- and macroscopic levels in this important class of refractory bcc materials.

A complete list for mathematical symbols used throughout this work is given in Table 1.

Table 1 List of symbols.

Symbol	Definition or meaning
F, F <sup>e</sup> , F <sup>p</sup>	Total, elastic, and plastic deformation gradients
Re, Ue	Elastic rotation, right stretch
Ce, Ee	Elastic right Cauchy-Green tensor, elastic strain tensor
$\mathbf{L}, \mathbf{L}^{e}, \mathbf{L}^{p}$	Velocity gradient, elastic and plastic distortion rates
$\dot{\gamma_{\rm p}}^{\alpha},\dot{\gamma_{\rm 0}}$	Plastic shear strain rate in the slip system $\alpha$ , reference slip rate
$\mathbf{m}_{0}^{\alpha}, \mathbf{n}_{0}^{\alpha}$	Slip direction and slip plane normal for slip system $\alpha$
$S_0^{\alpha}$ , $S^{\alpha}$	Schmid tensors in intermediate space and deformed configuration
$\mathbb{S}_{0,NS}^{i,\alpha}$	Non-Schmid projection tensors in intermediate space
Φ	Elastic free energy
c	Fourth-order elastic stiffness
$c_{11}, c_{12}, c_{44}$	Elastic constants at current temperature
$C_{11,0}, C_{12,0}, C_{44,0}$	Elastic constants at 0K
$m_{11}, m_{12}, m_{44}$	Slopes of the temperature-dependent elastic constants
A	Thermal expansion tensor
$\theta$ , $\theta_0$	Current and reference absolute temperatures
$\mu$ , $\mu_0$	Effective shear moduli at current temperature and 0K
$\mathbf{T}^e$ , $\mathbf{P}$ , $\mathbf{T}$	Elastic 2nd Piola stress, Piola stress, Cauchy stress
$\tau^{\alpha}, \tau^{\alpha}_{eff}$	Resolved shear stress, effective shear stress in slip system $\alpha$
$\tau_{ m NS}^{lpha},\widetilde{ au}_{eff}^{lpha}$	Resolved shear stress, effective shear stress including non-glide stresses
$\Delta G$	Activation energy
$k_B$	Boltzmann's constant
p, q	Parameters for the shape of stress-dependent kink-pair formation energy
$s^{\alpha}$ , $s_0$	Slip resistance in slip system $\alpha$ , far-field slip resistance
$\widetilde{s_l}, s_l$	Temperature-dependent lattice resistance, lattice resistance at 0K
5	Magnitude of Burgers vector
$a^{\alpha\beta}$	Dislocation interaction matrix
$o^{\alpha}$	Dislocation density in slip system $\alpha$
$\mathcal{L}^{\alpha}$	Mean free path of dislocation for slip system $\alpha$
$k_1, k_2$	Mean free path coefficients
$y_c^{\alpha}, y_{c0}$	Annihilation capture radius for slip system $\alpha$ , reference capture radius
$A_{rec}$	Capture radius energy
ρ	Material mass density
c	Specific heat
η	Taylor-Quinney factor

# 2. Single crystal behavior

## 2.1. Single crystal plasticity model

# 2.1.1. Kinematics

The deformation gradient is defined by,

$$\mathbf{F} = \operatorname{Grad} \mathbf{y},\tag{1}$$

where  $\mathbf{y} = \boldsymbol{\varphi}(\mathbf{X},t)$  is the spatial vector mapped via the motion,  $\boldsymbol{\varphi}$  and  $\mathbf{X}$  is the material vector in the reference configuration. Here, "Grad" denotes a gradient in the reference configuration. The deformation gradient multiplicatively decomposes into its elastic ( $\mathbf{F}^e$ ) and plastic ( $\mathbf{F}^p$ ) parts,

$$\mathbf{F} = \mathbf{F}^{\mathbf{e}} \mathbf{F}^{\mathbf{p}}.\tag{2}$$

The spatial velocity gradient represents the rate of deformation in the deformed configuration by,

$$\mathbf{L} = \operatorname{grad} \mathbf{v} = \dot{\mathbf{F}} \mathbf{F}^{-1},\tag{3}$$

where v is the spatial velocity field and "grad" is a gradient in the deformed configuration. The velocity gradient additively decomposes into elastic ( $L^e$ ) and plastic ( $L^p$ ) distortion rate tensors,

$$\mathbf{L} = \mathbf{L}^{e} + \mathbf{F}^{e} \mathbf{L}^{p} \mathbf{F}^{e-1}, \tag{4}$$

where  $L^e = \dot{F}^e F^{e-1}$  and  $L^p = \dot{F}^p F^{p-1}$ . Rearranging Eq. (4), we have,

$$\dot{\mathbf{F}}^{p} = \mathbf{L}^{p} \mathbf{F}^{p} \text{ with } \mathbf{F}^{p}(\mathbf{X}, 0) = \mathbf{1}.$$
 (5)

The dislocation motion is assumed to take place throughout prescribed slip systems  $\alpha=1\sim N$  in the lattice space. Here, we define the Schmid tensor  $\mathbb{S}_0^\alpha=\mathbf{m}_0^\alpha\otimes\mathbf{n}_0^\alpha$ , where  $\mathbf{m}_0^\alpha$  is the slip direction and  $\mathbf{n}_0^\alpha$  is the slip plane normal in the intermediate (or

lattice) space elastically relaxed from the deformed spatial configuration. Since plastic flow takes place throughout the prescribed slip systems, the plastic distortion rate tensor in the lattice space is expressed by,

$$\mathbf{L}^{\mathbf{p}} = \sum_{\alpha=1}^{N} \dot{\gamma_{\mathbf{p}}}^{\alpha} \mathbb{S}_{0}^{\alpha}. \tag{6}$$

Here,  $\gamma_p^{\alpha}$  is the plastic shear strain rate in each of the slip systems. Equivalently, the rate of plastic distortion is expressed in the deformed configuration by,

$$\overline{\mathbf{L}^{\mathbf{p}}} = \mathbf{F}^{\mathbf{e}} \mathbf{L}^{\mathbf{p}} \mathbf{F}^{\mathbf{e}-1} = \sum_{\alpha=1}^{N} \dot{\gamma_{\mathbf{p}}}^{\alpha} \mathbb{S}^{\alpha}, \tag{7}$$

where  $\mathbb{S}^{\alpha} = (\mathbf{F}^{\mathbf{e}} \mathbf{m}_{0}^{\alpha}) \otimes (\mathbf{F}^{\mathbf{e} \cdot \mathbf{T}} \mathbf{n}_{0}^{\alpha})$  is the Schmid tensor in the deformed configuration. Furthermore, plastic flow is incompressible since,

$$trL^{p} = 0. (8)$$

The elastic deformation gradient allows for the polar decomposition,

$$\mathbf{F}^{\mathbf{e}} = \mathbf{R}^{\mathbf{e}} \mathbf{U}^{\mathbf{e}},\tag{9}$$

where Re is the elastic rotation and Ue is the elastic right stretch. Then we define the elastic strain tensor as,

$$\mathbf{E}^{e} = \frac{1}{2}(\mathbf{C}^{e} - \mathbf{1}),\tag{10}$$

where  $C^e = F^{eT}F^e$  is the elastic right Cauchy–Green tensor. Thus, the elastic strain tensor is defined in the intermediate space.

#### 2.1.2. Constitutive equations

The elastic free energy in the intermediate space is defined by,

$$\boldsymbol{\Phi} = \boldsymbol{\Phi}(\mathbf{E}^{\mathbf{e}}, \boldsymbol{\theta}) = \frac{1}{2} \mathbf{E}^{\mathbf{e}} : \boldsymbol{C}[\mathbf{E}^{\mathbf{e}}] - (\boldsymbol{\theta} - \boldsymbol{\theta}_0) \mathbf{A} : \boldsymbol{C}[\mathbf{E}^{\mathbf{e}}].$$
(11)

Here, ": " denotes the inner product of two tensors. Then, the elastic 2nd Piola stress conjugate to Ee is obtained by,

$$\mathbf{T}^{e} = \frac{\partial \boldsymbol{\Phi}(\mathbf{E}^{e}, \boldsymbol{\theta})}{\partial \mathbf{E}^{e}} = \boldsymbol{C} \left[ \mathbf{E}^{e} - \mathbf{A}(\boldsymbol{\theta} - \boldsymbol{\theta}_{0}) \right], \tag{12}$$

where C is the fourth-order elastic stiffness tensor and A is the second order thermal expansion tensor. Moreover,  $\theta$  is the current absolute temperature and  $\theta_0$  is the reference temperature. The elastic 2nd Piola stress is related to the Piola stress P by,

$$\mathbf{P} = \mathbf{F}^{\mathbf{e}} \mathbf{T}^{\mathbf{e}} \mathbf{F}^{\mathbf{p}-\mathbf{T}}.\tag{13}$$

Then, it is also related to the Cauchy stress T, using the relation,  $T = J^{-1}PF^{T}$  with  $J = \det F$ ,

$$\mathbf{T}^{e} = J\mathbf{F}^{e-1}\mathbf{T}\mathbf{F}^{e-T}.$$

The resolved shear stress that drives slip on the  $\alpha$ -th slip system is projected from the elastic 2nd Piola stress via the Schmid tensor defined in the intermediate lattice space,

$$\tau^{\alpha} = \mathbf{C}^{\mathbf{e}} \mathbf{T}^{\mathbf{e}} : \mathbb{S}_{0}^{\alpha} \approx \mathbf{T}^{\mathbf{e}} : \mathbb{S}_{0}^{\alpha}, \tag{15}$$

since the elastic deformation is small in this work.

The plastic strain rate on the  $\alpha$ -th slip system is then constitutively prescribed by the form of the thermally-activated velocity of screw dislocations,

$$\dot{\gamma_{p}}^{\alpha} = \dot{\gamma_{0}} \exp\left(-\frac{\Delta G}{k_{B}\theta} \left\langle 1 - \left(\frac{\tau_{eff}^{\alpha}}{\widetilde{s_{l}}}\right)^{p} \right\rangle^{q}\right) \quad \text{for} \quad \tau_{eff}^{\alpha} > 0,$$

$$\text{otherwise} \quad \dot{\gamma_{p}}^{\alpha} = 0; \qquad \tau_{eff}^{\alpha} = |\tau^{\alpha}| - s^{\alpha},$$
(16)

where  $\tau^{\alpha}_{eff}$  is the effective shear stress,  $\dot{\gamma}_0$  is the reference slip rate,  $\Delta G$  is the activation energy,  $k_B$  is Boltzmann's constant,  $s^{\alpha}$  is the slip resistance from dislocation interaction, p and q denote the parameters for the shape of stress-dependent kink-pair formation energy, and  $\langle \,\cdot\, \, \rangle = \frac{1}{2} \left(\, |\cdot| + (\,\cdot\,)\, \right)$  is a Macaulay bracket. Furthermore, the temperature-dependent lattice resistance,  $\widetilde{s_l}$  is expressed by,

$$\widetilde{s}_l = s_l \frac{\mu}{\mu_0},\tag{17}$$

where  $s_l$  is the lattice resistance at 0 K and  $\mu_0 = \sqrt{C_{44,0} \left(\frac{C_{11,0} - C_{12,0}}{2}\right)}$  and  $\mu = \sqrt{C_{44} \left(\frac{C_{11} - C_{12}}{2}\right)}$  are the effective shear moduli at 0 K and current temperature, respectively.

# 2.1.3. Slip resistance and dislocation evolution

The phenomenological hardening law in classical crystal plasticity models was found to reasonably capture the strain-hardening behavior in bcc materials in various crystallographic orientations (Stainier et al., 2002; Cho et al., 2018). More recently, many

single crystal plasticity models for both fcc and bcc materials have employed a modified Taylor hardening law associated with the evolution of dislocation densities (Bronkhorst et al., 2019; Lim et al., 2020; Nguyen et al., 2021). In this work, we employ the modified Taylor hardening law to better represent the underlying physics for the evolution of dislocations and their interactions throughout the slip systems. The slip resistance in the  $\alpha$ -th slip system is expressed as,

$$s^{\alpha} = s_0 + \mu b \sqrt{\sum_{\beta=1}^{N} a^{\alpha\beta} \rho^{\beta}},\tag{18}$$

where  $s_0$  is the far-field resistance to slip,  $\mu$  is the effective shear modulus, b is the magnitude of Burgers vector and  $\rho^{\beta}$  is the dislocation density in each slip system,  $\beta$ . Moreover,  $a^{\alpha\beta}$  is the interaction matrix that characterizes the interaction strength between the slip systems  $\alpha$  and  $\beta$ , which will be further discussed below.

In order to compute the slip resistance in the modified Taylor hardening law (Eq. (18)), the dislocation density in each of the slip systems must be simultaneously computed via an appropriate evolution model. Numerous evolution models for computing the dislocation density exist in the literature for single crystal plasticity theories of bcc materials. Some bcc single crystal plasticity models have used a simple evolution rule for dislocation densities in which the interaction strengths between the slip systems were assumed to be equal (Knezevic et al., 2014; Lim et al., 2015). Moreover, there is literature on the bcc single crystal plasticity models in which the geometric features in dislocation interactions throughout the slip systems were taken into account. Ma and Roters (2004), Ma et al. (2007) proposed a simple model in which the forest and parallel dislocation densities associated with the slip resistance in a slip system ( $\alpha$ ) were computed such that dislocation densities in all other slip systems ( $\beta \neq \alpha$ ) were geometrically projected onto the central slip system (α). Their interpretation for geometry of dislocation interaction was recently employed to model single crystalline bcc tungsten (Cereceda et al., 2016) exhibiting anomalous yield features due to non-Schmid effects. More recently, Nguyen et al. (2021) modified the geometric interaction model of Ma, Roters and Raabe to account for evolution of forest and co-planar (including parallel) dislocation densities in which the mixed characteristics of edge and screw dislocations were taken into account. All of these models have found success in capturing some important features in the thermomechanical behavior of single crystal bcc materials in various crystallographic orientations. Yet, these models for bcc single crystal plasticity have limitation in accounting for the dislocation density evolution associated with interaction strengths strongly dependent on the type of interaction as well as the dependence of the dislocation interaction strengths on the hardening behavior.

Meanwhile, mesoscopic dislocation dynamics (dd) simulations have enabled computing the interaction properties of dislocations for which both short-range contact interactions and long-range elastic interactions are taken into account throughout the slip systems for single crystalline bcc materials (Queyreau et al., 2009; Madec and Kubin, 2017; El Ters and Shehadeh, 2019; Cui et al., 2020). Specifically, for both fcc and bcc crystals, the dd simulations have elucidated the roles of collinear interactions and various junctions in the slip activation processes as well as the hardening mechanisms throughout slip systems, as well postulated in Madec et al. (2003) and Devincre et al. (2005). Hence, a "soft" multi-scaling between the mesoscopic dd simulation and the macroscopic hardening law has enriched the physical picture in the continuum single crystal models in which the dislocation interaction strengths are explicitly taken into account (Dequiedt et al., 2015; Bronkhorst et al., 2019). In this work, we employ dd simulation results for tantalum to better represent the dislocation microstructures and interactions in the single crystal model.

The dislocation density in each of the slip systems in Eq. (18) is taken to evolve according to a multiplication–annihilation type model (Dequiedt et al., 2015),

$$\dot{\rho}^{\alpha} = \frac{1}{b} \left( \frac{1}{\mathcal{L}^{\alpha}} - 2y_{c}^{\alpha} \rho^{\alpha} \right) |\dot{\gamma_{p}}^{\alpha}|, \tag{19}$$

where  $\mathcal{L}^{\alpha}$  is the mean free path of dislocations, and  $y_c^{\alpha}$  is the annihilation capture radius. The mean free path is inversely proportional to the forest dislocation density, i.e.,

$$\frac{1}{\mathcal{L}^{\alpha}} = \sqrt{\sum_{\beta=1}^{N} d^{\alpha\beta} \rho^{\beta}} \tag{20}$$

with  $d^{\alpha\beta} = \frac{a^{\alpha\beta}}{k_1^2}$  for self interaction or coplanar interaction, and  $d^{\alpha\beta} = \frac{a^{\alpha\beta}}{k_2^2}$  for other interactions, where  $k_1$  and  $k_2$  are the mean free path coefficients. In this work, we employ the interaction strengths,  $a^{\alpha\beta}$ , informed by dd simulations for tantalum recently performed by Madec and Kubin (2017). Further detailed description of the dislocation interaction strengths employed in the single crystal model is provided together with other material parameters in Section 2.1.5. Moreover, the temperature and rate-dependent annihilation capture radius is expressed by,

$$y_c^{\alpha} = y_{c0} \left( 1 - \frac{k_B \theta}{A_{rec}} \ln \left| \frac{\dot{\gamma}_p^{\alpha}}{\dot{\gamma}_0} \right| \right), \tag{21}$$

where  $y_{c0}$  is the reference annihilation capture radius, and  $A_{rec}$  is the capture radius energy, following (Beyerlein and Tomé, 2008).

#### 2.1.4. Temperature evolution

It has been known that during plastic deformation of metallic materials, the plastic work is partitioned into stored energy of cold work and thermal energy (Taylor and Quinney, 1934). The energy stored in the atomic bond extension and contraction due

to the evolution of dislocation density and structure is significant. The proportion of plastic work partitioned into thermal energy is generally termed the Taylor–Quinney factor (Taylor and Quinney, 1934). Although it has been demonstrated that the Taylor–Quinney factor is very likely not constant and can take values substantially below 1.0 (Rittel et al., 2017; Lieou and Bronkhorst, 2020, 2021), doing so within the present structural theory is beyond the scope of this work and therefore is assumed to simply remain constant. The evolution of temperature is then taken as

$$\rho c \dot{\theta} = \eta \sum_{n=1}^{N} \tau^{\alpha} \dot{\gamma_{p}}^{\alpha}, \tag{22}$$

where  $\eta$  is the Taylor–Quinney factor,  $\rho$  is the material mass density, and c is the specific heat. Furthermore, it is assumed for strain rates below 1000 s<sup>-1</sup> that  $\eta = 0.0$  and above that  $\eta = 1.0$ . The Laplacian term in the original heat equation has also been neglected.

#### 2.1.5. Slip systems and material parameters

As noted in the introduction, screw dislocations in tantalum and other bcc metallic materials dissociate into non-planar partial dislocation configurations while at rest as a lower energy state. This creates ambiguity in the proper stress to use to drive dislocation motion as the partial dislocation configuration is believed to be composed of three Burgers vectors which form a triangle. To provoke motion of screw dislocations, the split core must be forced to become planar once again and given the triangular configuration of the partial dislocations, the stress conditions to do so are not directionally isotropic and set up a condition of twin and anti-twin directionality for the motion of these dislocations on any given slip system. Atomistic calculations of screw dislocation dissociation in a number of different bcc materials on the {110}(111) type of systems has been clearly demonstrated (Gröger et al., 2008a,b). Similar physical demonstration for the {112}(111) and {123}(111) types has not yet been made. Neither has the influence of the split dislocation core upon dislocation interactions been studied in bcc metals given the hypothesis that screw dislocation motion may be via the nucleation and propagation of kink-bands (Butler et al., 2018). We know from prior work that including both {110}(111) and {112}(111) types of slip systems as options for dislocation motion is necessary to properly describe crystallographic texture evolution (Kothari and Anand, 1998; Bronkhorst et al., 2006) with the role of {123}(111) systems within a continuum crystal mechanics setting unclear. Although, not yet well quantified, there are indications that the directional asymmetry described above is reduced with increase in material temperature (Sherwood et al., 1967). Prior work has estimated this to be noticeable but small at room temperature for tantalum (Cho et al., 2018; Bronkhorst et al., 2021). As further discussed in Section 2.3, the physical foundations for the non-Schmid effects on {112} slip planes are still lacking largely and the non-Schmid effects have been found to be negligible at room temperature and higher. Thus, in our analysis for the single crystal behavior at room temperature and higher presented in Section 2.2, we employ the classical Schmid tensor and the corresponding resolved shear stress at the primary external driving force for dislocation motion on the  $\{110\}\langle 111\rangle$  and  $\{112\}\langle 111\rangle$  types at these temperatures. Slip systems are listed in Tables 2 and 3.

Table 2
Slip systems for {110}(111).

onp systems for (110)(111).					
Slip system	$\mathbf{m}_0^{\alpha}$	$\mathbf{n}_0^{\alpha}$			
A2	[111]	(011)			
A3	$[\overline{1}11]$	(101)			
A6	$[\overline{1}11]$	(110)			
B2	[111]	$(0\overline{1}1)$			
B4	[111]	$(\bar{1}01)$			
B5	[111]	$(\bar{1}10)$			
C1	$[\overline{11}1]$	(011)			
C3	$[\overline{11}1]$	(101)			
C5	$[\overline{11}1]$	$(\bar{1}10)$			
D1	$[1\overline{1}1]$	(011)			
D4	$[1\overline{1}1]$	$(\bar{1}01)$			
D6	$[1\overline{1}1]$	(110)			

Table 3 Slip systems for  $\{112\}\langle 111\rangle$ .

Slip system	$\mathbf{m}_0^{\alpha}$	$\mathbf{n}_0^{\alpha}$
A <u>4</u>	[111]	(211)
A <u>8</u>	$[\overline{1}11]$	$(\bar{1}1\bar{2})$
A <u>11</u>	$[\overline{1}11]$	$(\overline{121})$
B <u>3</u>	[111]	$(\bar{2}11)$
B <u>7</u>	[111]	$(11\bar{2})$
B12	[111]	$(1\bar{2}1)$
C <u>2</u>	$[\overline{11}1]$	$(\overline{112})$
C <u>5</u>	$[\overline{11}1]$	$(\bar{1}21)$
C10	$[\overline{11}1]$	$(2\overline{1}1)$
D <u>1</u>	$[1\overline{1}1]$	$(1\overline{12})$
D6	$[1\overline{1}1]$	(121)
D <u>9</u>	$[1\overline{1}1]$	$(\overline{211})$

The material parameters used in the model are listed in Table 4. The mass density  $\rho$ , specific heat c, and thermal expansion tensor  $A = \alpha 1$  are assumed to be constant during deformation. The fourth-order elastic stiffness tensor is expressed in terms of the three independent elastic constants ( $C_{11}$ ,  $C_{12}$ ,  $C_{44}$ ). The elastic constants are linearly dependent on temperature as  $C_{ii} = C_{ii.0} + m_{ii}\theta$ .  $\{C_{11,0}, C_{12,0}, C_{44,0}\}$  at 0 K and  $\{m_{11}, m_{12}, m_{44}\}$  are assumed to follow the previous work by Kothari and Anand (1998), Cho et al. (2018) and Bronkhorst et al. (2021). The values of  $\dot{\gamma}_0$ ,  $\Delta G$ ,  $s_I$  and p and q in the flow model are identified based on the previous work that employed similar single crystal models for tantalum (Kothari and Anand, 1998; Cho et al., 2018; Bronkhorst et al., 2021). Then, these values have been further tuned to better capture the rate-dependent stress-strain behaviors in the single crystals.

Table 4 Material parameters used in this study

material parameters used in this study.						
$\rho$ [kg/m <sup>3</sup> ]	16 640	$a_{ m J}$	0.05			
c [J/kg-K ]	150	$a_{ m XJ}$	0.04			
$\alpha$ [ $\mu$ m/m-K]	6.5	$s_0$ [MPa]	35.0			
$k_b$ [J/K]	$1.38 \times 10^{-23}$	$\dot{\gamma_0}$ [sec <sup>-1</sup> ]	$1.0 \times 10^{7}$			
$C_{11,0}$ [GPa]	268.5	$\Delta G$ [J]	$2.1 \times 10^{-19}$			
$C_{12,0}$ [GPa]	159.9	$s_l$ [MPa]	400.0			
$C_{44,0}$ [GPa]	87.1	$\sum_{\alpha} \rho_0^{\alpha} [m^{-2}]$	$2.4 \times 10^{12}$			
$m_{11}$ [MPa/K]	-24.5	$y_{c0}$	6 <i>b</i>			
$m_{12}$ [MPa/K]	-11.8	$A_{rec}$ [J]	$2.0 \times 10^{-20}$			
$m_{44}$ [MPa/K]	-14.9	p	0.28			
$a_{\text{copl}}$	0.06	q	1.34			
a <sub>colli 60°</sub>	0.7744	$k_1$	180			
$a_{\mathrm{colli}90^{\circ}}$	0.9025	$k_2$	2.5			
a <sub>colli 30°</sub>	0.5112	b [nm]	0.286			

The dislocation interaction coefficients are taken to follow the work by Madec and Kubin (2017). Instead of using the full asymmetric interaction matrices throughout the slip systems of  $\{110\}\langle111\rangle$  and  $\{112\}\langle111\rangle$ , we further simplified the interaction coefficients, as follows.

- $a_{\text{copl}} = 0.06$  for the self- and coplanar interactions,
- $a_{\text{colli}\,60^\circ} = 0.7744$  for the collinear interaction and  $\theta = \arccos|\mathbf{n}_0^\alpha \cdot \mathbf{n}_0^\beta| = 60^\circ$ ,  $a_{\text{colli}\,90^\circ} = 0.9025$  for the collinear interaction and  $\theta = \arccos|\mathbf{n}_0^\alpha \cdot \mathbf{n}_0^\beta| = 90^\circ$ ,
- $a_{\text{colli} 30^{\circ}} = 0.5112$  for the collinear interaction and  $\theta = \arccos |\mathbf{n}_0^{\alpha} \cdot \mathbf{n}_0^{\beta}| = 30^{\circ}$ ,
- $a_{\rm J} = 0.05$  for the junctions between {110} systems or {112} systems,
- $a_{XJ} = 0.04$  for the junctions between {110} and {112} systems.

As pointed out in Queyreau et al. (2009), the presence of friction stress due to alloy friction or lattice resistance can screen the elastic field between dislocations. Thus, this culminates in a decrease in the line-tension and interaction strengths. Since the lattice resistance has been taken into account in our single crystal model, the values for the junction strengths  $(a_J, a_{XJ})$  are taken to be slightly smaller than the average junction strengths determined in Madec and Kubin (2017).

The values for the remaining parameters,  $s_0$ ,  $y_{c0}$ ,  $A_{rec}$ ,  $k_1$ , and  $k_2$  are then identified using the experimental data for the single crystal behaviors at low to high strain rates and for the polycrystal behavior at low strain rate in through-thickness direction.

The finite deformation single crystal model was numerically implemented for use in a finite element solver (a standard branch of Abaqus) for boundary value problems of single- and polycrystalline tantalum discussed in the next sections. We implemented the implicit multi-step computational procedure for updating the stress tensor, kinematic tensors and all of the state variables including the dislocation densities evolving together with deformation, following and modifying the algorithms proposed by Kalidindi et al. (1992). Furthermore, we computed a fourth-order tangent tensor also known as the Jacobian consistent with the viscoplastic single crystal model used in a Newton-type iteration for obtaining a solution that satisfies the global equilibrium at the end of the increment in the nonlinear boundary value problems. All the details regarding the implicit time integration procedure and the computation of tangent are provided in Appendices A and B, respectively.

Furthermore, we have solved the boundary value problems for both single and polycrystal behaviors using the finite element procedures. When inhomogeneous deformation fields are expected (e.g. [149] single crystal and examples in Section 2.3.2), we have employed a cylindrical domain consisting of a number of finite elements, where we have used a hexahedral element with reduced integration. The top and bottom surfaces of the cylindrical samples are constrained to remain parallel and the lateral surfaces are free to move. Furthermore, these boundary conditions have been further verified through more simulations with periodic boundary conditions for both single and polycrystal cases with inhomogeneous deformation fields (Anand, 2004; Danielsson et al., 2002; Hansen et al., 2010). Meanwhile, when the deformation is homogeneous especially in high symmetric orientations (e.g. [001] and [011] directions), we have conducted simple single-element simulations.

# 2.2. Single crystal behavior at low to high strain rate and at room temperature and higher

Here, we validate the finite deformation single crystal model without non-Schmid effect presented above against experimental data for high purity single crystal tantalum (99.99%). We used the single crystal stress-strain data at low to high strain rates recently published by Rittel et al. (2009), Whiteman et al. (2019), Lim et al. (2020) and Nguyen et al. (2021).

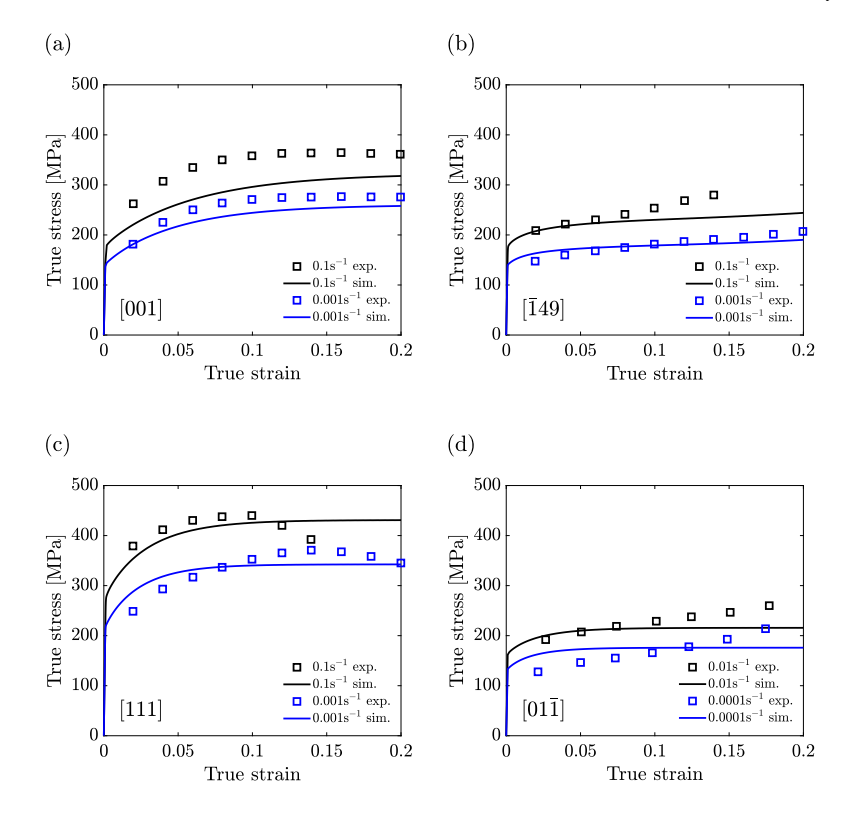


Fig. 1. Stress-strain behavior of single crystal tantalum in experiments and numerical simulations at low strain rates and at room temperature: (a) [001], (b)[149], (c) [111] and (d) [011] in compression. The single crystal data were taken from Lim et al. (2020) and Rittel et al. (2009).

Fig. 1 shows the measured and numerically simulated stress–strain curves for single crystalline tantalum in crystallographic orientations of [001],  $[01\bar{1}]$ , [111] and  $[\bar{1}49]$  at strain rates of 0.001 s<sup>-1</sup> and 0.1 s<sup>-1</sup> and at room temperature without any non-Schmid effects. As evidenced in the figures, the model captures well the main features of the rate-dependent yield and flow stresses for the various crystallographic orientations. The highest initial yield point and the flow stresses in the [111] orientation due to the lowest Schmid factor are nicely described by the model. Furthermore, the hardening behavior and its tendency toward larger strains are reasonably well captured in the [001], [111] and  $[\bar{1}49]$  orientations. However, in the  $[01\bar{1}]$  orientation, the hardening behavior observed in the experiment is poorly predicted by the model. This discrepancy can likely be attributed to crystallographic misorientation<sup>1</sup> or some finite size effects in samples during experimentation. Additionally, the stress–strain behavior in this particular  $[01\bar{1}]$  orientation has large variations amongst the experimental data reported by different research groups (Rittel et al., 2009; Whiteman et al., 2019; Lim et al., 2020).

In Fig. 2, the single crystal behavior is further presented at high strain rates in both experiments and numerical simulations. The high strain rate curves are displayed for room temperature and higher in the crystallographic orientations of [001] (Fig. 2a), [01 $\bar{1}$ ] and [111] (Fig. 2b). The orientation- and temperature-dependent yield stress and flow stresses are excellently captured by the model. Furthermore, the single crystal model captures nicely the thermal softening that manifests due to adiabatic heating under high strain rate conditions. In summary, the present crystal model has been shown to be capable of capturing the main features of the orientation-dependent stress–strain behaviors of single crystal tantalum at low (0.001 s<sup>-1</sup>) to high ( $\sim$  5000 s<sup>-1</sup>) strain rates and at room (296K) to high (873K) temperatures.

### 2.3. Single crystal behavior with non-Schmid effect at low temperature

#### 2.3.1. Slip instability in $\{110\}\ \langle 111 \rangle$ slip systems

The collinear interactions taken into account in the present single crystal model have been found to be critical for predicting active slip systems in fcc single crystals loaded in high symmetry orientations (e.g.  $\langle 100 \rangle$ ,  $\langle 110 \rangle$  and  $\langle 111 \rangle$ ), as posited by Madec et al. (2003) and Devincre et al. (2005). Notably, as further discussed in recent dislocation dynamics studies (Queyreau et al., 2009;

<sup>&</sup>lt;sup>1</sup> As pointed out by Cuitiño and Ortiz (1993) and Stainier et al. (2002), for single crystal specimens with high symmetric orientation along the loading direction, small misalignment in the loading axis breaks the symmetry of resolved shear stress, resulting in a significant change in slip activity and stress responses.

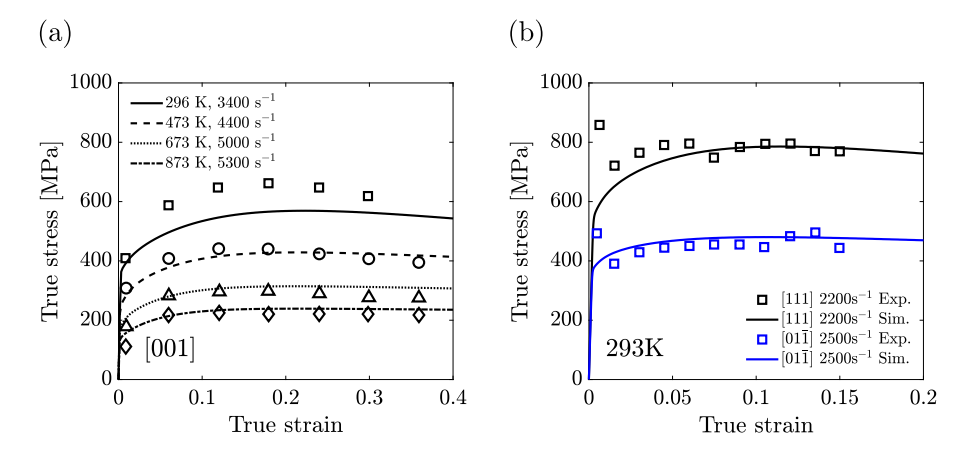


Fig. 2. Stress–strain behavior of single crystal tantalum in experiments (open symbols) and numerical simulations (lines) at high strain rate compression. (a) [001] at room temperature to higher (b) [011] and [111] at high strain rates. The single crystal data were taken from Nguyen et al. (2021) and Whiteman et al. (2019).

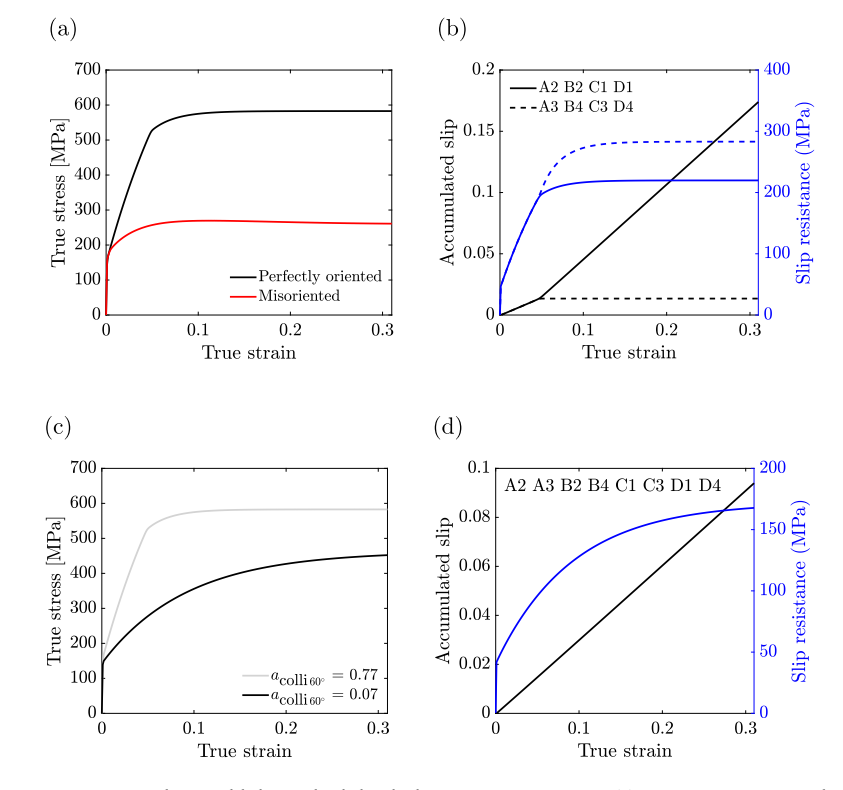


Fig. 3. Effect of collinear interactions on single crystal behavior loaded in high symmetry orientations. (a) Stress-strain curves with and without misorientation, (b) evolution of accumulated slip and slip resistance without misorientation, (c) stress-strain curves and (d) accumulated slip and slip resistance with a weaker collinear interaction and without misorientation.

Madec and Kubin, 2017), the collinear interactions were found to be strong in bcc materials. Moreover, in Madec and Kubin (2017), from which we have taken the interaction strength for tantalum, the strength of collinear interactions throughout the  $\{110\}$  slip systems have been found to be markedly strong. Hence, we analyze the role of collinear interactions in the slip activation processes for tantalum single crystals. We numerically examine instability induced by strong collinear interactions, especially on  $\{110\}$  slip planes. Towards this end, we excluded the 12  $\{112\}$   $\{111\}$  slip systems in the numerical simulations for single crystals.

Fig. 3 shows a numerically simulated stress–strain responses of a tantalum single crystal loaded in a high symmetry orientation of [001], together with accumulated slip and slip resistances in eight slip systems having the same Schmid factor. Here, (A3, A2), (B4, B2), (C3, C1) and (D4, D1) are the pairs of slip systems collinear-interacting on the {110} slip planes. As shown in Fig. 3b, though the accumulated slip in these eight slip systems evolve initially at the same rate, they bifurcate after a small amount of

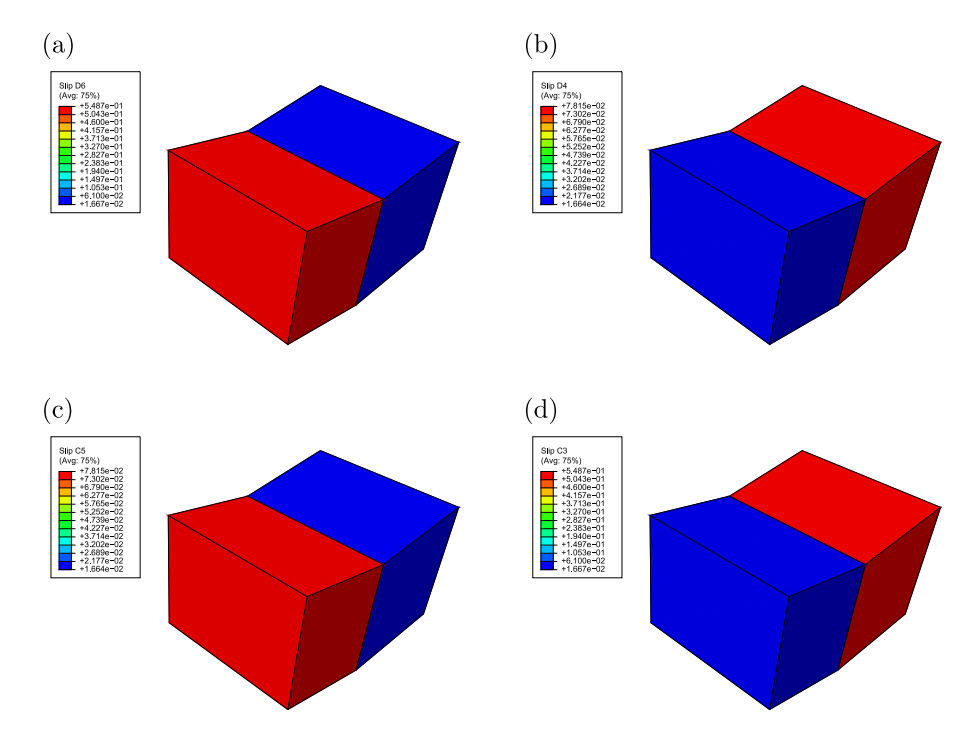


Fig. 4. Accumulated slip on four equivalent slip systems in a single crystal loaded in [011]. (a) D6, (b) D4, (c) C5 and (d) C3, in the two element simulation.

deformation. Interestingly, in the deactivated cross-slip systems (A3, B4, C3 and D4), the slip resistance continues to evolve. While, in the active slip systems (A2, B2, C1 and D1), the slip resistance does not evolve significantly since their cross-slip counterparts become deactivated (See the modified Taylor hardening law in Eq. (18)). Instability in the slip activation process was found to culminate in an anomalously stiff response beyond the initial yield as shown in Fig. 3a (black solid line with no misorientation). Such an anomalous stress response sustains until the collinear interactions vanish due to the lattice distortion in the deformed single crystal. Next, we introduced a slight misorientation (0.6°) between the sample axis and the loading direction. The slight misorientation resulted in asymmetry in the initial Schmid factors (or resolved shear stresses) for the eight slip systems. The asymmetry due to the slight misorientation culminated in early determination for activation without any bifurcation throughout the equivalent slip systems. As evidenced in the simulated stress–strain curve (red solid line in Fig. 3a), the abnormally stiff response observed in the perfectly oriented sample diminishes with misorientation. Then, the single crystal response in this high symmetry orientation without any precursor for instability. The stable hardening behavior is evidenced by Fig. 3d on slip resistances and accumulated slip in the equivalent eight slip systems. These slip systems having the same Schmid factor are equally active without any bifurcation during deformation. All of these simple numerical results clearly reveal that the collinear interactions throughout the  $\{110\}$   $\{111\}$  slip systems play a critical role in determining slip activation processes in bcc single crystals loaded in high symmetry orientations.

Slip instability is further addressed in a single crystal loaded in another high symmetry direction, the  $[01\bar{1}]$  orientation, where only four equivalent slip systems, here two collinear pairs of "C3 and C5" and "D4 and D6", are possibly activated. We conducted a simple two-element simulation for a single crystal loaded in this particular orientation. Fig. 4 shows accumulated slip on initially equivalent four slip systems (D6, D4, C5 and C3 for Fig. 4a, b, c and d, respectively) at a compressive strain of 0.3. Active slip systems are bifurcated spatially throughout the two elements in order to avoid the strong collinear interactions and the resulting zig-zag type deformation develops. This simple numerical result also reveals that possible manifestation of sub-grain events such as grain fragmentation (Berger et al., 2022) or formation of dislocation cell blocks (Noell et al., 2017) due to instability in the bcc single crystals in multi-slip situations.

In order to improve our mechanistic understanding of the slip instability and bifurcation due to the strong collinear interactions, we performed an analysis on the energy landscape in the single crystal loaded in the  $[01\bar{1}]$  orientation illustrated in Fig. 4. To this end, we calculated an incremental work density through numerical integration of the stress power,

$$\dot{W} = \mathbf{P} : \dot{\mathbf{F}} = \mathbf{P} : \mathbf{LF},$$

$$= \mathbf{T}^{\mathbf{e}} : \dot{\mathbf{E}}^{\mathbf{e}} + \sum_{\alpha=1}^{N} \tau^{\alpha} \dot{\gamma_{\mathbf{p}}}^{\alpha}.$$
(23)

Since the elastic stretch is negligibly small, we consider only the plastic part of the stress power  $(\dot{W}^p = \sum_{\alpha=1}^N \tau^\alpha \dot{\gamma}_p^\alpha)$ . In the single crystal loaded in the [01 $\bar{1}$ ] direction, the four slip systems of C3, C5, D4 and D6 are initially equivalent and lattice rotation is

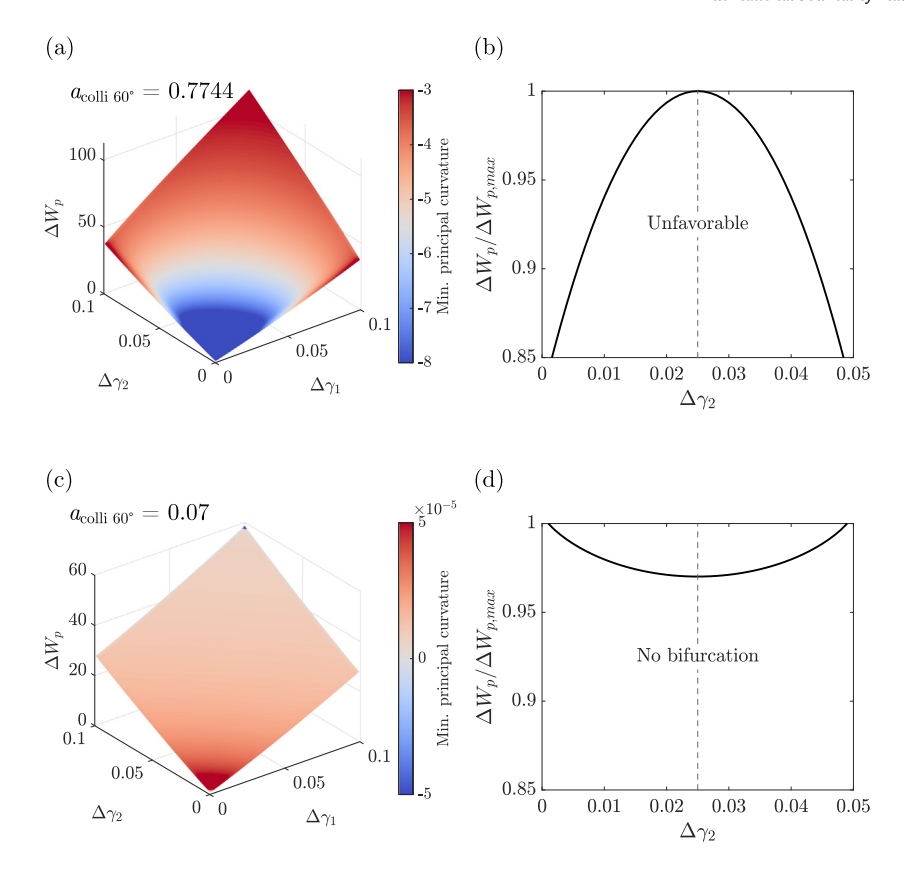


**Fig. 5.** Incremental plastic work density and its principal curvature as functions of  $Δγ_1$  and  $Δγ_2$  with (a) stronger collinear interaction ( $a_{\text{colli}60^\circ} = 0.7744$ ) and (c) weaker collinear interaction ( $a_{\text{colli}60^\circ} = 0.07$ ). Incremental plastic work density plotted with fixed total slip rate ( $Δγ_1 + Δγ_2 = 0.05$ ) for (c) stronger collinear interaction ( $a_{\text{colli}60^\circ} = 0.7744$ ) and (d) weaker collinear interaction ( $a_{\text{colli}60^\circ} = 0.07$ ).

suppressed due to symmetry and geometric constraint. Then, in each of the two elements, only one in the two collinear-interacting slip systems (collinear pairs of C3 and C5; and D4 and D6) is more activated; i.e., the {C3, D4} and {C5, D6} slips are bifurcated into the two elements as shown in Fig. 4. Based upon these numerical observations, we make the following assumptions for incremental slip in the {C3, D4} and {C5, D6} slip systems,

$$\Delta \gamma_1 = \Delta \gamma_{C3} = \Delta \gamma_{D4},$$

$$\Delta \gamma_2 = \Delta \gamma_{C5} = \Delta \gamma_{D6}.$$
(24)

With the fixed slip increments in Eq. (24), the plastic part of the incremental work density can be calculated by

$$\Delta W^p = \sum_{\alpha=1}^N \tau^\alpha \Delta \gamma_p^\alpha. \tag{25}$$

The resolved shear stress is calculated using the flow rule with the fixed slip increments and slip resistances. The dislocation densities of the four active slip systems (C3, C5, D4 and D6) are assumed to be  $1 \times 10^{13}$  m<sup>-2</sup>; and those of inactive slip systems are assumed to be  $2 \times 10^{11}$  m<sup>-2</sup>. Then, the plastic incremental work density in Eq. (25) is numerically integrated using the trapezoidal rule. Fig. 5 shows the calculated incremental plastic work density as a function of  $\Delta \gamma_1$  and  $\Delta \gamma_2$ , where the color on the surface indicates the minimum principal curvature of the incremental plastic work density. As shown in Fig. 5a, the minimum principal curvature was found to be negative for any slip increments with the strong collinear interaction strength ( $a_{colli60^\circ} = 0.7744$ ). Negative curvature in the incremental plastic work density is more clearly evidenced in Fig. 5b where the total slip increment is taken to be fixed ( $\Delta \gamma_1 + \Delta \gamma_2 = 0.05$  here). Negative curvature of the incremental plastic work density displayed in Figs. 5a and b implies that homogeneous slip activation throughout the four equivalent systems (i.e.,  $\Delta \gamma_{C3} = \Delta \gamma_{C5} = \Delta \gamma_{D4} = \Delta \gamma_{D6}$ ) is energetically unfavorable. The slip bifurcation is inevitable, attributed to the failure to find a unique, energy-minimizing solution. The incremental plastic work density is then calculated with a weaker collinear interaction strength. As revealed in Fig. 5c and d, the weaker collinear interaction resulted in a convex incremental plastic work density (non-negative curvature in the incremental work); the stable, homogeneous slip with no bifurcation throughout the equivalent slip systems is favorable for an energy-minimizing deformation process.

Finally, we further illustrate slip instability and spatial inhomogeneity in the deformation field in the single crystal subjected in uniaxial tension in the  $[01\bar{1}]$  direction. In order to trigger "spatial" instability, we applied an orientation defect (1°) to the

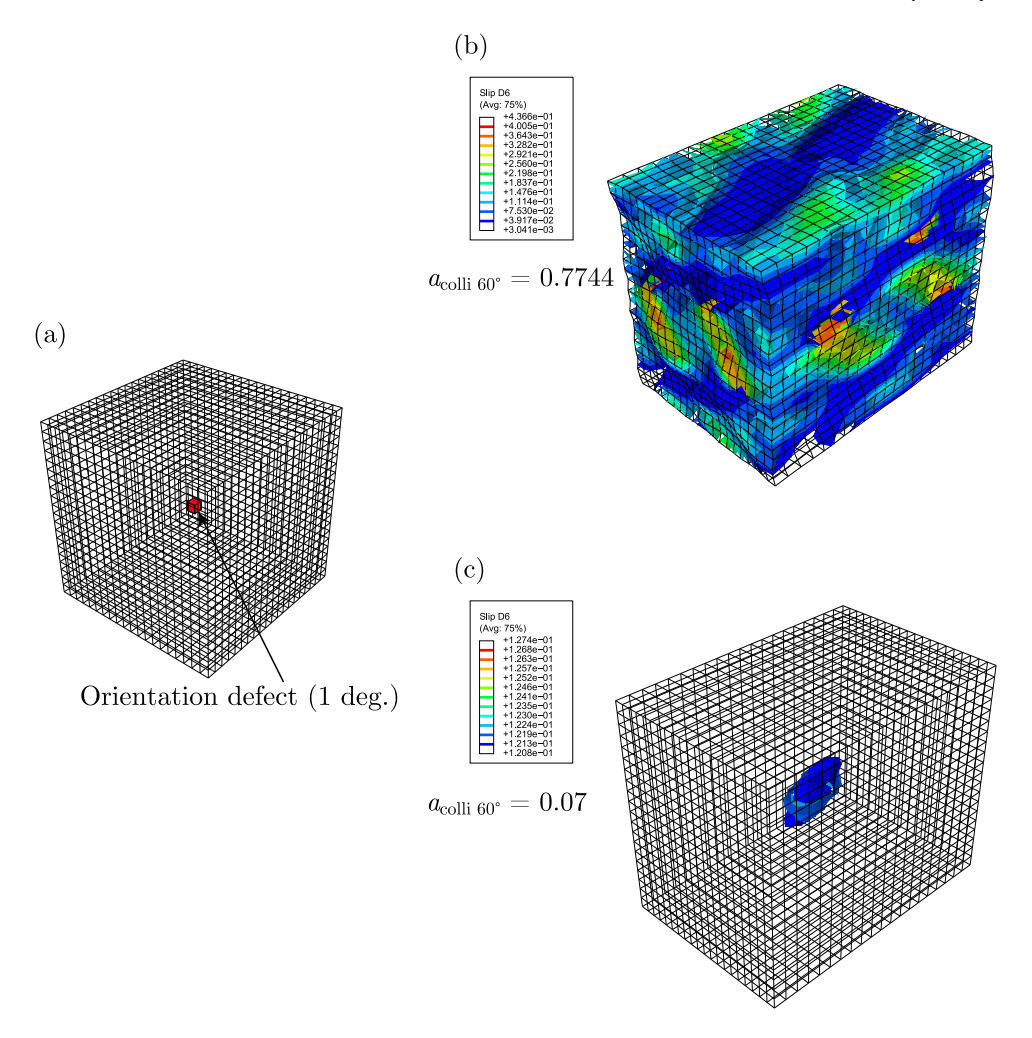


Fig. 6. Spatial inhomogeneity and instability in a single crystal loaded in [01 $\bar{1}$ ] due to a spatial orientation defect. (a) Defect (1°) in a finite element mesh and iso-surfaces of an accumulated slip in a slip system of D6 with (b) strong collinear interaction ( $a_{\text{colli}60^\circ} = 0.7744$ ) and (c) weaker collinear interaction ( $a_{\text{colli}60^\circ} = 0.07$ ).

central element in a finite element mesh for the single crystal as illustrated in Fig. 6a. Figs. 6b and c show the iso-surfaces of an accumulated slip in a slip system of D6 with the collinear interaction strengths of 0.7744 and 0.07, respectively. When the collinear interaction is strong, a significant deformation inhomogeneity propagates from the central defect throughout the finite element mesh, as shown in Fig. 6b; i.e., the deformation inhomogeneity accompanied by spatial slip bifurcation is energetically more favorable than the homogeneous deformation through equal activation in all possible slip systems. In contrast, as shown in Fig. 6c with the weaker collinear interaction strength, the deformation inhomogeneity never develops throughout the finite element mesh; i.e., the deformation field in this situation is stable and homogeneous against a spatial perturbation. In order to aid visualization for the instability induced by the strong collinear interactions throughout  $\{110\}$   $\langle 111 \rangle$  slip systems at low temperature, we have provided movie clips on propagation of the instability triggered by a small geometric perturbation in the single crystal loaded in high symmetric orientation,  $[01\bar{1}]$ , as a Supplementary Material. See Videos S1 and S2 in Supplementary Material.

If the additional  $\{112\}$  slip systems are included, no slip systems in collinear interactions are activated in single crystal samples loaded in the high symmetric orientations of  $\langle 100 \rangle$ ,  $\langle 110 \rangle$  and  $\langle 111 \rangle$ . Hence, no instability is observed as we demonstrated in Fig. 1 on the room temperature single crystal behavior with the 24 slip systems. Slip instability that possibly emanates from the latent hardening in multi-slip situations throughout the  $\{110\}$   $\langle 111 \rangle$  slip systems in the single crystals loaded in high symmetry orientations is associated as well with the non-Schmid behavior discussed in the following Section 2.3.2.

## 2.3.2. Non-Schmid behavior: Experiments vs. model

Since the early studies by Christian (1983), the breakdown of the Schmid law has been widely investigated for the group V and VI bcc transition metals. Numerous atomistic simulation studies with non-central interatomic potentials capable of capturing mixed nature of free-electron and covalent characteristics have revealed that the cores of  $1/2 \langle 111 \rangle$  screw dislocations spreading onto

several different  $\{110\}$  planes in the  $\langle 111 \rangle$  zone are responsible for the non-Schmid behavior. The non-Schmid effects involve the dependence of critical resolved shear stress on the orientation of the maximum resolved shear stress plane strongly associated with the twinning/anti-twinning asymmetry as well as tension–compression asymmetry of the yield stress. The non-Schmid effects in tantalum and all other bcc transition metals have been found to be most pronounced on the  $\{110\}$   $\langle 111 \rangle$  slip systems, for which the majority of the previous studies have focused on anomalous glide of the screw dislocations especially on the  $\{110\}$  planes. Only a few recent studies have explored the non-Schmid effects on the  $\{112\}$   $\langle 111 \rangle$  slip systems, by which empirical models for anomalous slip on the  $\{112\}$  planes have been constructed (Knezevic et al., 2014; Savage et al., 2017, 2018; Zecevic and Knezevic, 2018). Most recently, the tension–compression asymmetry on the  $\{112\}$   $\langle 111 \rangle$  slip systems have been further explored in Nguyen et al. (2021), in which the Peierls stress difference between twinning and anti-twinning slip directions on the  $\{112\}$  planes was assumed to be one of the major sources of non-Schmid effects within bcc metals. Although, in these earlier modeling studies on bcc materials, the possible anomalous slip on the  $\{112\}$   $\langle 111 \rangle$  slip systems has been introduced, the non-Schmid effects on these  $\{112\}$  planes should be much further studied via experiments and numerical simulations.

Of particular interest is also identifying slip systems in bcc transition metals over a range of temperatures and strain rates. The physical picture for complex slip in bcc crystals has been studied as well in numerous experiments and atomistic simulations, by which it has been very clear that slip occurs in the closest packed (111) direction. However, identifying the planes where slip occurs still remains a significant challenge. As posited in several important reviews on the active slip planes in tantalum and other bcc metals (Seeger, 2001; Weinberger et al., 2013; Weygand et al., 2015), slip almost always occurs predominantly on the {110} planes at low temperatures. As temperature increases, slip is observed on the {110}, {112} and {123} planes at room temperature and higher. Furthermore, slip is extensively observed on the maximum resolved shear stress planes; i.e., the non-Schmid effects diminish significantly at room temperature and higher. The transition temperature from the {110} to the {112} slip has been found to be between 100 K and room temperature especially for tantalum materials (Seeger, 1995, 2001; Weinberger et al., 2013). However, there is still ambiguity on activity of the {110} or {112} slip especially around room temperature, as recently argued in Lim et al. (2021), where dominant dislocation slip on the {112} planes were experimentally observed in tantalum single crystals under compression at room temperature. All of the previous experimental and theoretical studies on the slip planes have revealed slip occurs predominantly on the {110} planes in tantalum at low temperatures. Furthermore, slip on the {110} planes is strongly associated with the anomalous behavior of the  $\langle 111 \rangle$  screw dislocations non-planar throughout three-fold  $\{110\}$  planes. Additionally, the latent hardening possibly due to the strong collinear interactions throughout the {110} (111) slip systems may lead to slip instability and spatial bifurcation in the multi-slip situations in tantalum single crystals loaded in high symmetry orientations, as shown in the previous section (Section 2.3.1). Hence, it should be noted that we herein place emphasis on the non-Schmid effects most apparent on the {110} (111) slip systems in tantalum especially at low temperatures below 100 K. To this end, we extend the dislocation density-based single crystal plasticity model presented in Section 2.1, to account for the non-Schmid behavior involving tension-compression asymmetry in tantalum single crystals especially loaded in high symmetry orientations.

Based upon the three-term formulation on the non-Schmid stresses (Gröger et al., 2008a,b; Cho et al., 2018), we define the modified resolved stress ( $\tau_{NS}^{\alpha}$ ) for each of the slip systems,

$$\tau_{NS}^{\alpha} = \mathbf{T}^{e} : \widetilde{\mathbb{S}}^{\alpha} = \mathbf{T}^{e} : (\mathbb{S}_{0}^{\alpha} + w_{1} \mathbb{S}_{0,NS}^{1,\alpha} + w_{2} \mathbb{S}_{0,NS}^{2,\alpha} + w_{3} \mathbb{S}_{0,NS}^{3,\alpha}), \tag{26}$$

where  $\mathbb{S}_0^{\alpha}$  is the Schmid tensor, and  $\mathbb{S}_{0.NS}^{1,\alpha}$ ,  $\mathbb{S}_{0.NS}^{2,\alpha}$  and  $\mathbb{S}_{0.NS}^{3,\alpha}$  are the non-Schmid projection tensors defined by,

$$\mathbb{S}_{0,\text{NS}}^{1,\alpha} = \mathbf{m}_0^{\alpha} \otimes \mathbf{n}_0^{\prime \alpha},\tag{27}$$

$$\mathbb{S}_{0,\text{NS}}^{2,\alpha} = (\mathbf{n}_0^{\alpha} \times \mathbf{m}_0^{\alpha}) \otimes \mathbf{n}_0^{\alpha},\tag{28}$$

$$\mathbb{S}_{0,\mathrm{NS}}^{3,\alpha} = (\mathbf{n}_0^{\prime \alpha} \times \mathbf{m}_0^{\alpha}) \otimes \mathbf{n}_0^{\prime \alpha},\tag{29}$$

where  $\mathbf{m}_0^{\alpha}$  is the slip direction,  $\mathbf{n}_0^{\alpha}$  is the slip plane normal and  $\mathbf{n}_0'^{\alpha}$  is the plane normal whose angle with the primary slip plane  $(\mathbf{n}_0^{\alpha})$  is 60 deg. Moreover,  $w_1$ ,  $w_2$  and  $w_3$  are the weighting factors for the non-glide stresses,  $\mathbf{T}^{\mathbf{e}}:\mathbb{S}_{0,\mathrm{NS}}^{1,\alpha}$ ,  $\mathbf{T}^{\mathbf{e}}:\mathbb{S}_{0,\mathrm{NS}}^{2,\alpha}$ , and  $\mathbf{T}^{\mathbf{e}}:\mathbb{S}_{0,\mathrm{NS}}^{3,\alpha}$  that represent the shear stress components parallel and perpendicular (the last two non-glide stresses) to the slip direction in the corresponding {110} planes. Detailed procedures to identify the weighting factors with some constraints can be found in Gröger and Vitek (2019).

The flow rule is also modified from Eq. (16)

$$\dot{\gamma_{p}}^{\alpha} = \dot{\gamma_{0}} \exp\left(-\frac{\Delta G_{0}}{k_{B}\theta} \left\langle 1 - \left(\frac{\widetilde{\tau_{eff}}^{\alpha}}{\widetilde{s_{l}}}\right)^{p} \right\rangle^{q}\right) \quad \text{for} \quad \widetilde{\tau_{eff}}^{\alpha} > 0 \quad \text{and} \quad \tau^{\alpha} > 0,$$

$$\text{otherwise} \quad \dot{\gamma_{p}}^{\alpha} = 0,$$
(30)

where  $\tilde{\tau}_{eff}^{\alpha}$  (=  $\tau_{NS}^{\alpha}$  -  $s^{\alpha}$ ) is the effective stress. To capture asymmetry of the yield stress, the sign of the resolved shear stress should be taken into account. Hence, the flow rule is modified to enable only positive slip. The slip systems used in the single crystal model with non-Schmid effects are given in Table 5. Due to the condition for positive slip, slip systems  $\alpha$  and  $\alpha$  + 12, which are equivalent within the Schmid law, cannot be simultaneously activated.

Table 5 Slip systems for the non-Schmid effect based model (Gröger et al., 2008b).

α	$\mathbf{m}_0^{\alpha}$	$\mathbf{n}_0^{\alpha}$	$\mathbf{n}_0^{\prime a}$	α	$\mathbf{m}_0^a$	$\mathbf{n}_0^{\alpha}$	$\mathbf{n}_0^{\prime a}$
1	[111]	$(\bar{1}0\bar{1})$	(110)	13	[111]	$(\bar{1}0\bar{1})$	(011)
2	$[\bar{1}11]$	(011)	(101)	14	$[1\overline{11}]$	(011)	$(\overline{110})$
3	$[\overline{1}11]$	(110)	$(01\bar{1})$	15	$[1\overline{11}]$	(110)	(101)
4	[111]	$(01\overline{1})$	$(\bar{1}10)$	16	$[\overline{111}]$	$(01\overline{1})$	$(10\overline{1})$
5	[111]	$(\bar{1}01)$	$(0\overline{1}1)$	17	$[\overline{111}]$	$(\bar{1}01)$	$(\bar{1}10)$
6	[111]	$(1\bar{1}0)$	$(10\bar{1})$	18	[111]	$(1\bar{1}0)$	$(0\overline{1}1)$
7	$[\overline{11}1]$	(011)	$(1\bar{1}0)$	19	$[11\overline{1}]$	$(0\overline{11})$	$(\bar{1}0\bar{1})$
8	$[\overline{11}1]$	(101)	(011)	20	$[11\overline{1}]$	(101)	$(1\overline{1}0)$
9	$[\overline{111}]$	$(\bar{1}10)$	$(\overline{1}0\overline{1})$	21	$[11\overline{1}]$	$(\bar{1}10)$	(011)
10	$[1\overline{1}1]$	(011)	$(\bar{1}01)$	22	$[\overline{1}1\overline{1}]$	(011)	(110)
11	$[1\overline{1}1]$	$(10\bar{1})$	(110)	23	$[\overline{1}1\overline{1}]$	$(10\overline{1})$	$(0\overline{11})$
12	$[1\overline{1}1]$	$(\overline{110})$	$(0\overline{11})$	24	$[\overline{1}1\overline{1}]$	$(\overline{110})$	(101)

Figs. 7a and 7b show the stress–strain curves for tantalum single crystals in tension and compression in [001] and [01 $\bar{1}$ ] orientations at 77 K, respectively. Since the single crystal samples were loaded in high symmetry orientations, slight misorientation (0.6 deg) is again introduced in order to avoid the undesirably stiff, unstable behavior accompanied by the slip bifurcation due to the strong interactions between collinear pairs on the {110} slip planes. The highly asymmetric yield stresses in both orientations are reasonably captured by the extended single crystal model without any further modifications on the material parameters. However, as shown in Fig. 7b on the single crystal loaded in  $[01\bar{1}]$  orientation, beyond the initial yield, the stress hardening especially in compression is much lower in the numerical simulation. The undesirable strain softening-like behavior is attributed to significant grain rotation as displayed in Fig. 8a. Furthermore, an unexpected overshoot in the stress response was observed in tension. Though the homogeneous misorientation throughout all elements enabled avoiding the slip instability, it was found to lead to significant crystallographic reorientation that gave rise to the globally unstable hardening behavior (e.g. Asaro (1983), Ortiz and Repetto (1999)).

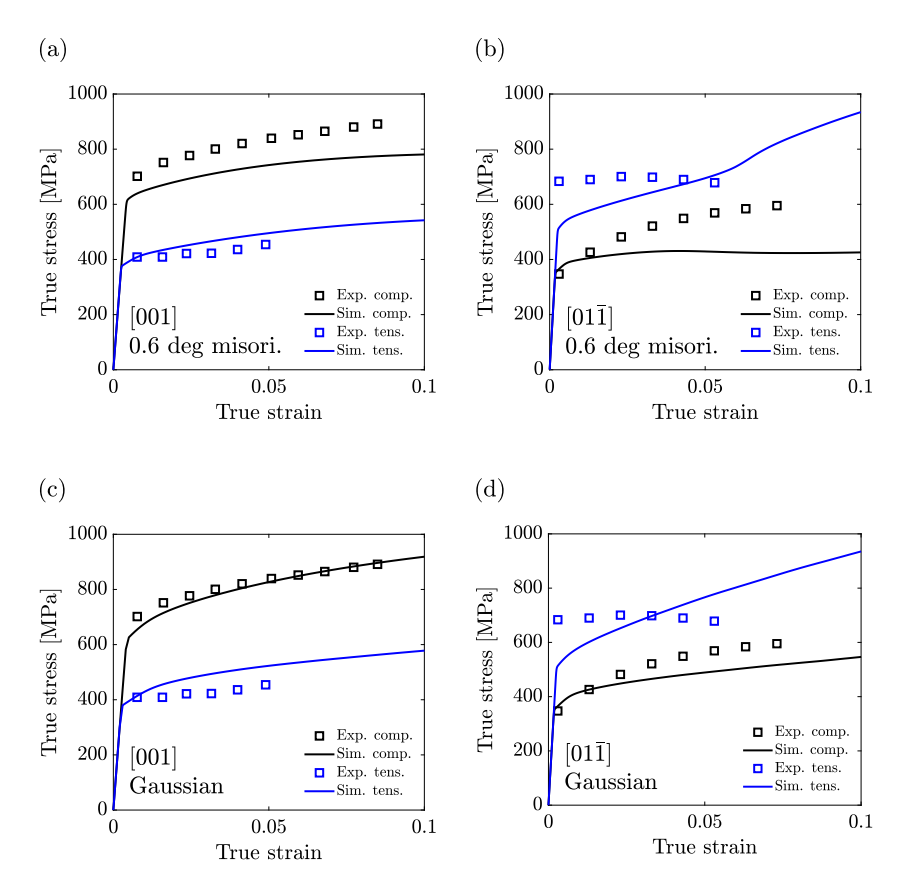


**Fig. 7.** Stress–strain behavior of single crystal tantalum in experiments and numerical simulations at low temperature (77 K and 0.001 s<sup>-1</sup>): (a) [001] and (b)  $[01\overline{1}]$  with 0.6 ° misorientation in both tension and compression. (c) [001] and (d)  $[01\overline{1}]$  with random misorientation in both tension and compression. Weighting factors ( $w_1$ ,  $w_2$  and  $w_3$ ) for non-glide stresses are 0.5, 0.2, and 0.1, respectively.

Source: Experimental data for high purity tantalum (99.99%) were taken from Sherwood et al. (1967).

The effect of the misorientation associated with instability is further investigated in Figs. 7c and 7d. Here, misorientation was randomly assigned to each of the elements, for which the Gaussian distribution with a standard deviation of 0.25 for  $\phi$  and 0.4 for  $\theta$  was employed for Canova convention Euler angles. As shown in the stress–strain curves, the extended single crystal model nicely captures overall features in the yield and hardening behavior without any stress overshoot and softening instability especially in compression in the  $[01\bar{1}]$  orientation. Furthermore, as shown in Fig. 8b, the crystallographic orientation  $[01\bar{1}]$  was found to be maintained with no significant grain rotation during deformation.

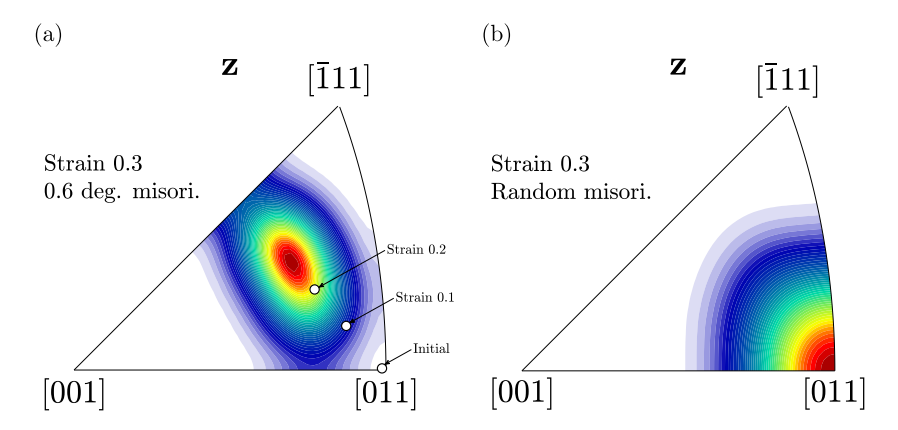


Fig. 8. Evolution of crystallographic orientations in single crystals in compression in  $[01\bar{1}]$  orientation. (a) Single crystal with 0.6 ° misorientation and (b) single crystal with randomly assigned misorientation, at a strain of 0.3. White makers in (a) indicate the mean orientations at initial and strains of 0.1 and 0.2.

In order to provide more generalized guidance for determining the non-Schmid factors, we present the numerically simulated stress–strain curves for tension and compression along [001], [01 $\bar{1}$ ], and [111] directions with varying  $w_1$ ,  $w_2$  and  $w_3$  in Fig. 19 in Appendix C.

Furthermore, tension–compression asymmetry diminishes significantly at room temperature and higher. Our single crystal model is also capable of capturing the decrease in the tension–compression asymmetry of the yield stresses by taking the weighting factors to be functions of temperature, i.e.,  $w_i = w_{i.SS} + (w_{i.OK} - w_{i.SS}) \exp(-\theta/\theta_r)$ , where  $w_{i.OK}$  are the weighting factors at 0 K,  $w_{i.SS}$  is the saturation weighting factor, and  $\theta_r$  is the characteristic temperature that controls of the rate of decaying in the weighting factors. Here,  $w_{i.OK}$  are taken to be 1.00, 0.41 and 0.20 for i = 1, 2, 3, respectively. In addition,  $w_{i.SS}$  is taken to be 5% of the  $w_{i.OK}$ .  $\theta_r$  is taken to be 100 K. The simulated yield stresses are displayed in Fig. 9. By simply introducing the saturation-type non-Schmid factors, our single crystal model captured the temperature-dependent yield stresses in both tension and compression, where the degree of asymmetry diminishes toward room temperature.

#### 3. Polycrystal behavior

The deformation mechanisms in polycrystal tantalum have been investigated, traced back to the early work by Chen and Gray (1996), Nemat-Nasser et al. (1998) and Kothari and Anand (1998). In these classical papers, the highly temperature- and rate-dependent inelastic features in polycrystal tantalum were addressed. Furthermore, the polycrystal models that employed the phenomenological hardening law were found to capture well some features in flow stresses and crystallographic texturing without any notion of dislocation evolution and interaction. This success with the phenomenological hardening law has been deemed due to the macroscopic hardening responses not sensitive to the details of dislocation evolution and interaction throughout the polycrystalline network.

Here, the single crystal model presented in Section 2 is further underpinned by examining the predictive capabilities of the model for polycrystal tantalum. To this end, we conducted mechanical tests for polycrystal tantalum samples machined in two different directions (through-thickness and in-plane) taken from the wrought tantalum plate. Furthermore, *ex situ* measurements on crystallographic texture evolution in the deformed samples at increasing strains were conducted. In addition to crystallographic texture, dislocation density was monitored using *ex situ* neutron diffraction measurements. The polycrystalline behavior involving stress–strain responses, dislocation density evolution and texture evolution is then reproduced in numerical simulations in which the single crystal plasticity model is employed without any further modification. The results below show the predictive capabilities of our modeling framework on both single- and polycrystal tantalum materials at low to high strain rate and at room temperature and higher.

# 3.1. Experiment

Multiple cylindrical high purity tantalum (99.99%) specimens of 4.2 mm diameter and 8.4 mm length were electro-discharge machined from a wrought plate with their axes parallel to either the through-thickness (TT) or in-plane (IP) directions. IP polycrystal

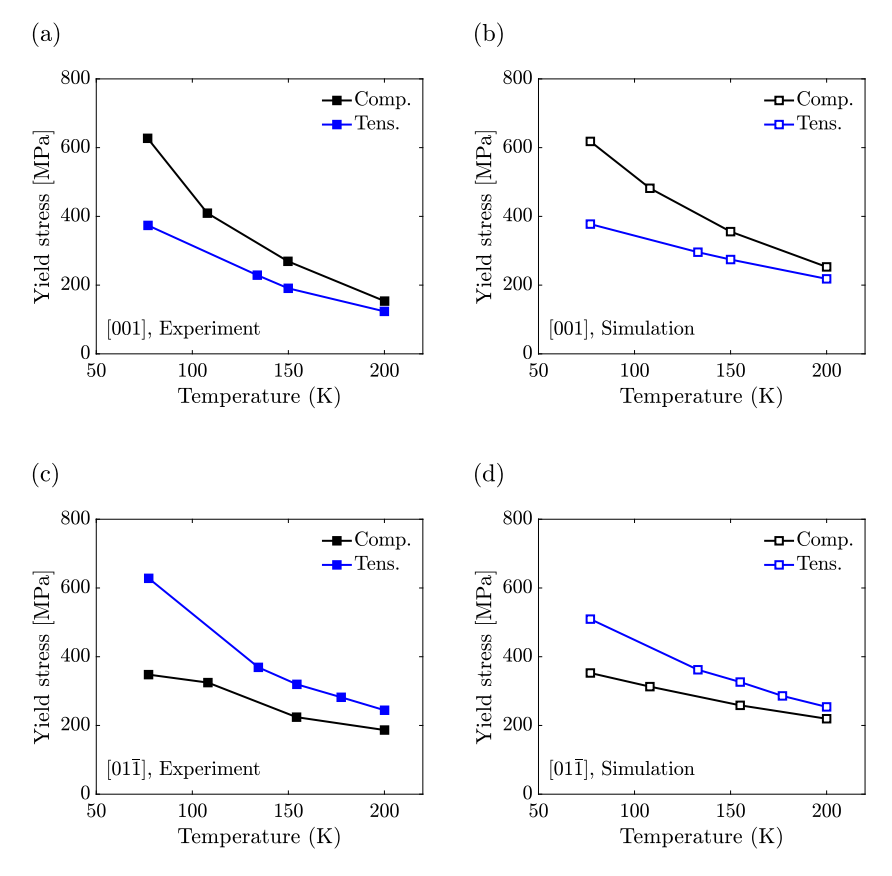


Fig. 9. Temperature-dependent yield stress under tension and compression. (a) Experiment, (b) model along [001] orientation, (c) experiment, (d) model along [011] orientation.

tantalum specimens were compressed in-situ at a strain rate of  $0.001 \text{ s}^{-1}$  to maximum true strain levels of 0.08, 0.18, 0.44, 0.89 or 0.149. In parallel, the TT and IP specimens were compressed *ex situ* to compressive true strains of 0.2, 0.3 and 0.4.

Bulk texture measurements of the specimens were conducted on the High-Pressure/Preferred Orientation (HIPPO) neutron time-of-flight diffractometer (Wenk et al., 2003; Vogel et al., 2004) at the Lujan Center at the Los Alamos Neutron Science Center (LANSCE). HIPPO consists of 1,200  $^3$ He detector tubes on 45 panels arranged on five rings around the incident neutron beam with nominal diffraction angles of 144°, 120°, 90°, 60°, and 40° covering 22.4% of  $4\pi$  (Takajo and Vogel, 2018). The deformed samples at strains of 0.2, 0.3 and 0.4 were glued on to sample holders with their cylinder axis along the holder axis and loaded on an automated robotic sample changer on HIPPO (Losko et al., 2014). Data was then collected at three rotations around the sample axis of 0°, 67.5°, and 90°. Data over a d-spacing range from 0.7 Å to 2.5 Å was analyzed with the Rietveld method (Rietveld, 1969) as implemented in the Materials Analysis Using Diffraction (MAUD) code following procedures described previously (Wenk et al., 2010). The orientation distribution was represented by the E-WIMV method (Matthies et al., 2005) using a resolution of 7.5°. From the MAUD analysis, pole figure data recalculated from the refined ODF was exported for further processing.

High-resolution (FWHM ~0.1%), high-statistics time-of-flight (TOF) neutron diffraction data was collected on the Spectrometer for MAterials Research at Temperature and Stress (SMARTS) for the purpose of diffraction line profile analysis (DLPA) (Brown et al., 2016) of each of the deformed specimens. The extended convolutional multiple whole profile (eCMWP) method (Ribárik et al., 2004) was used for semi-quantitative determination of the dislocation density in each of the deformed tantalum specimens. Annealed copper foil was used to determine the instrumental resolution and a Pearson VII function was used to fit the individual peak profiles to determine the breadth and shape parameters.

# 3.2. Stress-strain behavior, crystallographic texturing and dislocation density evolution

Numerical simulations for polycrystalline tantalum are conducted in which each of the finite elements represents one crystal. We use a finite element model comprising  $1000 (10 \times 10 \times 10; \text{Fig. } 10a)$  hexahedral elements with reduced integration. Furthermore, the single crystal modeling framework with both  $\{110\}$  and  $\{112\}$  slip systems without any non-Schmid effects presented in Section 2.2 has been employed to simulate the polycrystal behavior at room temperature and higher and at low to high strain rates. For simple compression, all faces are constrained to remain parallel, and displacement boundary conditions corresponding to loading conditions

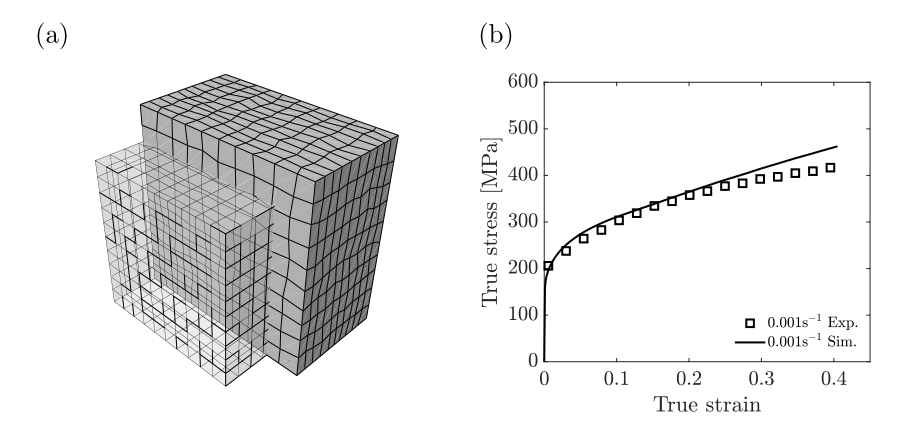


Fig. 10. (a) polycrystal model in undeformed (transparent) and deformed (gray) configurations, (b) stress–strain response in experiment and numerical simulation under loaded along the through-thickness direction at  $0.001~\rm s^{-1}$  and  $300~\rm K$ .

are applied on the top surface. The initial texture in each of the through-thickness and the in-plane direction was extracted from the measured data using MTEX (Bachmann et al., 2010) and the corresponding set of Euler angles ( $\phi$ ,  $\theta$  and  $\omega$ ) was then randomly assigned to each of the elements in order to represent the initial material texture.

Fig. 10 shows the response of polycrystal tantalum in compression (strain rate:  $0.001 \text{ s}^{-1}$ ) in both experiment and numerical simulation. Together with undeformed and deformed meshes shown in Fig. 10a, the measured and numerically simulated stress strain curves along the through-thickness direction are displayed in Fig. 10b. As shown, the numerically simulated responses including yield stress and overall hardening behavior are in good agreement with the measured data.

Figs. 11 and 12 shows a comparison of the pole figures from experiments and numerical simulations of the polycrystal tantalum under compression along the through-thickness and in-plane directions respectively. The sample in the through-thickness direction was found to be initially textured in the (100) and (111) as shown in Fig. 11a at zero strain. In addition, the sample in the in-plane

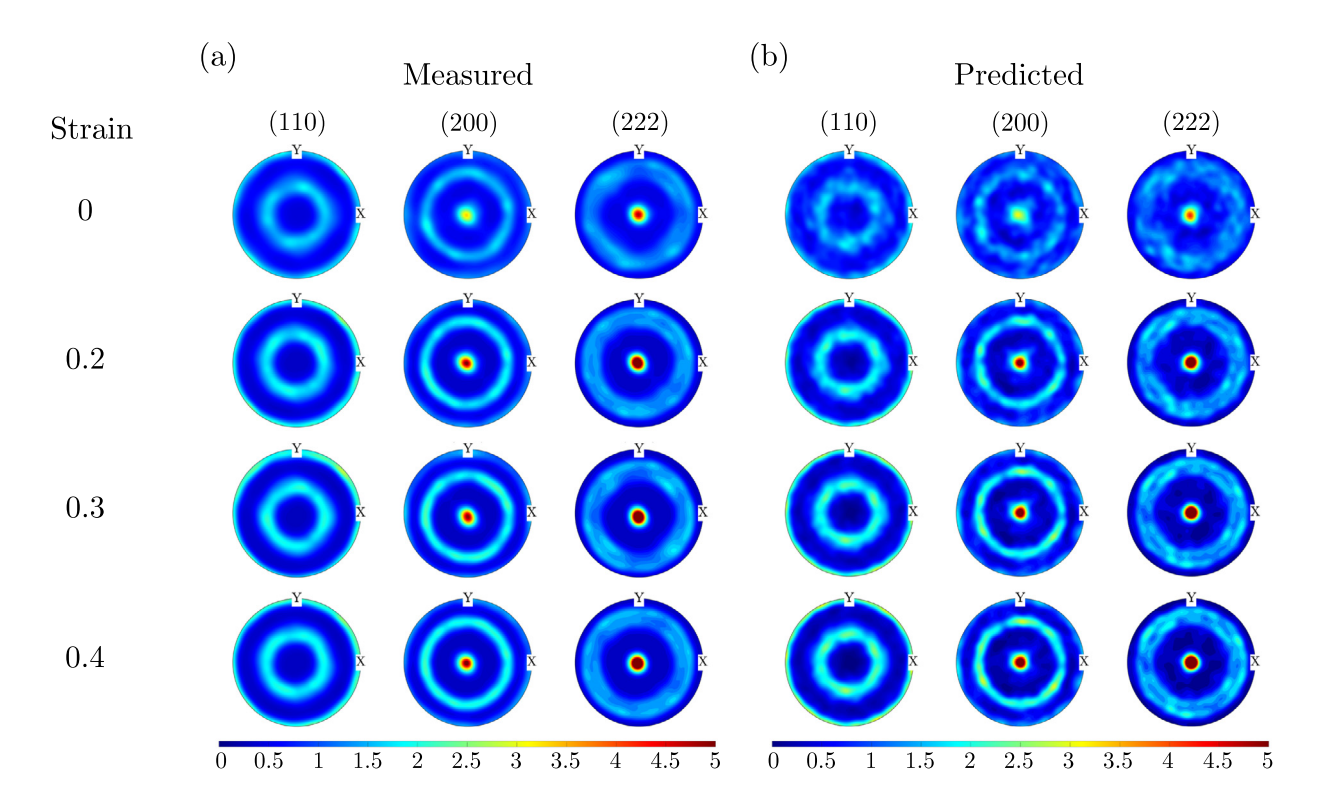


Fig. 11. Texture evolution during compression along the through-thickness direction. Pole figures (a) measured and (b) numerically predicted.

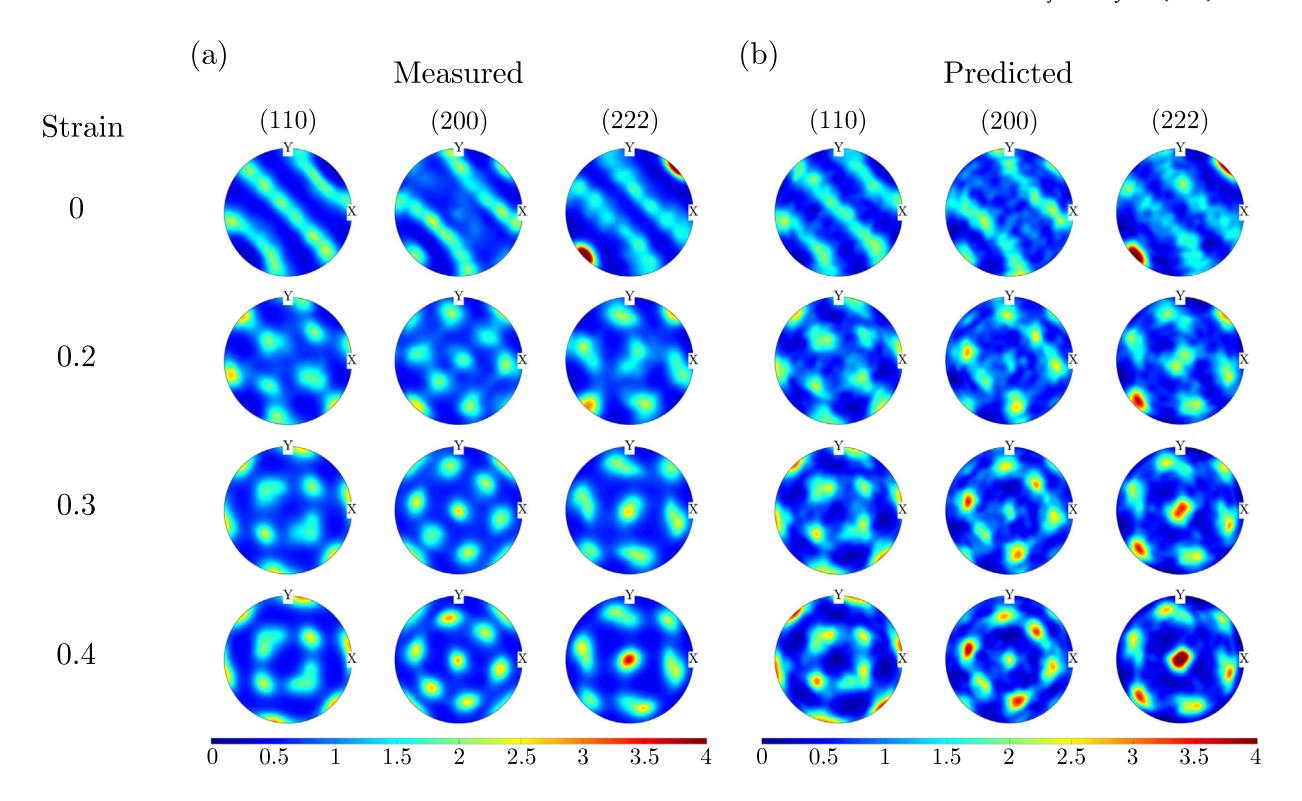


Fig. 12. Texture evolution during compression along the in-plane direction. Pole figures (a) measured and (b) numerically predicted.

direction was found to be textured in the (110) direction as shown in Fig. 12a at zero strain. The texture development toward the (100) and (111) orientations is attributed to constrained rotations of grains by prescribed slip systems (Kocks et al., 1998), well predicted in our numerical simulations for both sample directions. Moreover, as recently pointed out in Lim et al. (2020) the rotation characteristics in bcc crystals are strongly dependent upon the types of the prescribed slip systems. Our experimental and numerical results on the texture evolution strongly support that the prescribed slip systems on both {110} and {112} planes have been appropriately chosen for this study.

We then directly compared the dislocation densities measured in our *ex situ* neutron diffraction experiments to those predicted in our numerical simulations in the through-thickness direction (Fig. 13a) and the in-plane direction (Fig. 13b). To this end, we plotted the flow stresses in the two sample directions as functions of dislocation density and imposed strain. Here, since the volume change is small, the total dislocation density is simply calculated by averaging the dislocation density at each integration point in the polycrystal model. As shown, our numerical simulations capture reasonably well the relations between dislocation densities and macroscopic stress and strain responses in both sample directions in terms of trend. Furthermore, the flow stresses are linearly dependent on the square root of the averaged dislocation density in both experiments and numerical simulations. However, the overall stress response in the numerical simulation especially in the in-plane direction is found to be higher than that in the experiment. This discrepancy is presumably attributed to a lack of information on initial distributions of dislocation densities for numerical simulations and not yet adequately representing the complexities of dislocation dynamics and intergranular interaction in the materials.

# 3.3. High strain rate and high temperature behavior

Fig. 14 shows the stress–strain behavior of polycrystal tantalum in compression at high strain rates (> 10<sup>3</sup> s<sup>-1</sup>) in both experiments and numerical simulations. The high strain rate data was collected using a split-Hopkinson pressure bar system. The model predicts the overall strain rate dependence in yield and flow stresses at low to high temperature reasonably well. Notably, the remarkable decrease in yield stress with increasing temperature is well captured. Furthermore, as shown in Fig. 14b, the numerical simulations predict the low- to high strain rate behavior in polycrystal tantalum at room temperature reasonably well. Although the overall features in high strain rate and high temperature behaviors are reasonably predicted, the hardening behaviors at room temperature and 473 K are poorly captured in the numerical simulations. It is presumably attributed to inaccuracy in the interaction properties computed from the dislocation dynamics simulations especially at large strains and at high strain rates.

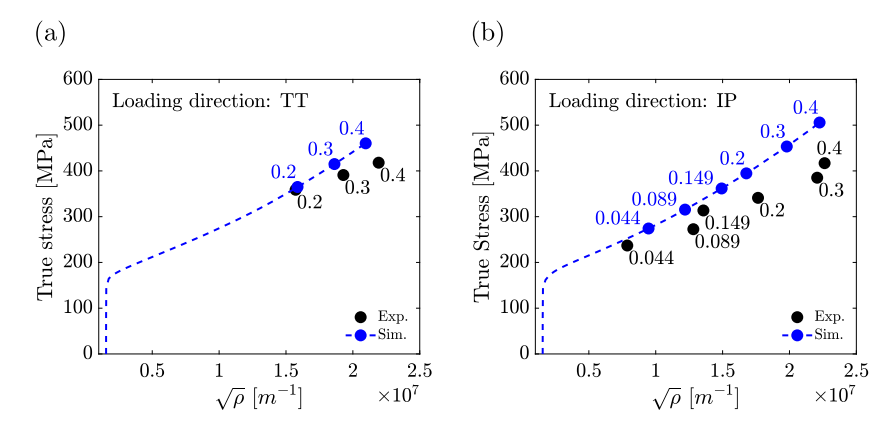


Fig. 13. Comparison between dislocation densities measured and numerically predicted for (a) through-thickness direction and (b) in-plane direction. Numerical values indicate true strain magnitude.

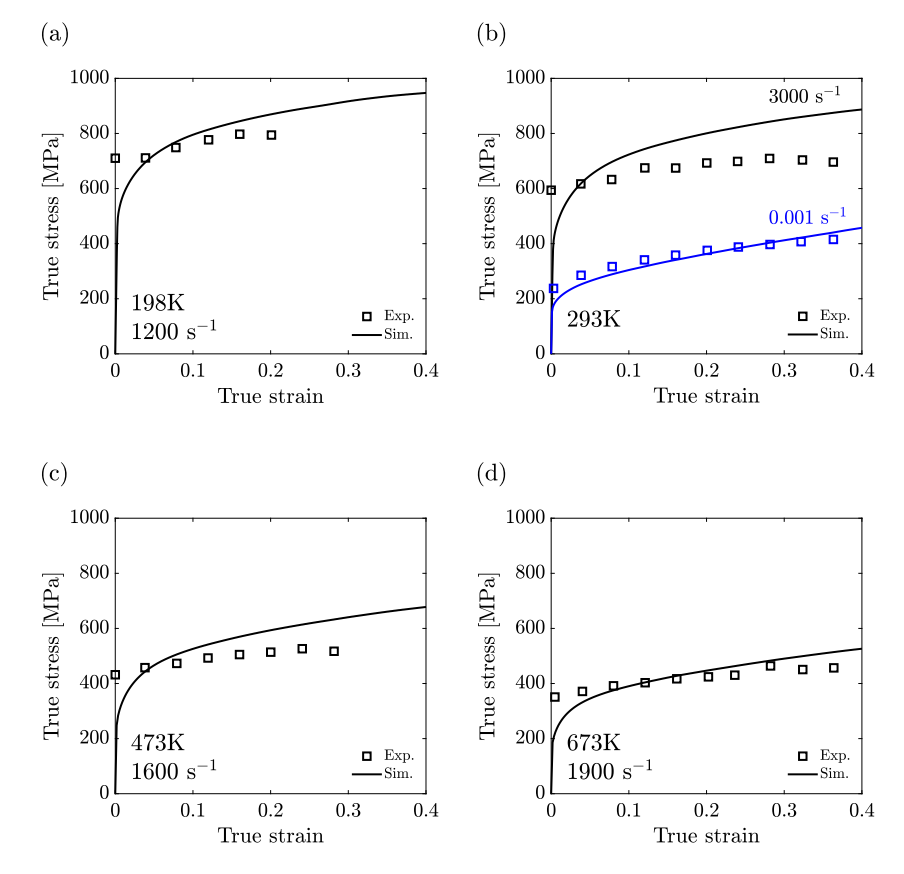


Fig. 14. Stress–strain behavior of polycrystal tantalum in experiments and numerical simulations at high strain rates and high temperatures: (a) at 198 K 1200 s<sup>-1</sup>, (b) at 298 K 0.001 s<sup>-1</sup> and 3000 s<sup>-1</sup>, (c)at 473 K 1600 s<sup>-1</sup>, and (d) at 673 K 1900 s<sup>-1</sup> in compression.

## 3.4. Grain-level analysis for rotation and dislocation density evolution

The macroscopic features in dislocation density, crystallographic texturing and stress–strain responses in polycrystal tantalum samples have been found to be captured well by the simple polycrystal model in which each element represented one crystal. Here, the polycrystal behavior is further addressed by numerical simulations on a polycrystal model based on Voronoi-tessellation. Though this Voronoi-tessellation-based polycrystal model is not grain-boundary conforming, it enables analysis of the local variations of dislocation density, slip activity, stress and rotation throughout more realistic polycrystalline network not available in the simple polycrystal model presented in Section 3.2.

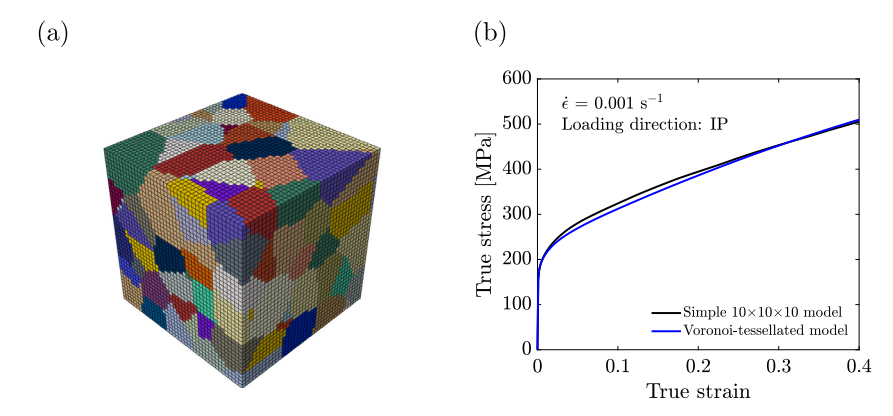


Fig. 15. (a) Voronoi-tessellation-based polycrystal model with 200 random spatial points (b) comparison of stress–strain curves between  $10 \times 10 \times 10$  polycrystal model and Voronoi model in the in-plane direction.

Fig. 15a shows a Voronoi-tessellated unit-cube with 200 random spatial Voronoi points. The tessellated domain is meshed with the hexahedral elements via voxelization using an open-source program, Neper (Quey et al., 2011). Moreover, the number of random Voronoi points has been chosen such that the Voronoi model reproduces the texture evolution captured by the simple polycrystal model (the set of  $10 \times 10 \times 10$  hexahedral elements) displayed in Fig. 12. In the Voronoi-tessellation-based polycrystal model, each of the polyhedral Voronoi cells represents one crystal to which a set of Euler angles extracted from the experiment is assigned. Then we conducted numerical simulations for the polycrystal domains under large compression. As shown in Fig. 15b, the macroscopic stress–strain curve in the Voronoi-tessellation-based polycrystal model matches well with that for the simple polycrystal model in the in-plane direction.

In the Voronoi-tessellation-based polycrystal model, three grains have been selected for detailed analysis for a intragranular behavior. The grain A initially oriented in the  $[4\bar{1}9]$  direction was selected since the location in the standard triangle has the maximum Schmid factor on the  $\{110\}$  slip planes (Fig. 16a). Under deformation, as shown in Fig. 16b, the grain tends to rotate toward the edge (between [001] and  $[1\bar{1}1]$  of the standard triangle) and then toward [001] such that the Schmid factor of the initially active slip system decreases along the corresponding great circle. Furthermore, a significant variation in rotation (or intragranular orientation) is observed inside the grain, as shown in Figs. 16b and 16c. Herein, the intragranular misorientation is computed via,  $\Delta g_i = g_i \langle g_{avg} \rangle^{-1}$ , where  $\Delta g_i$  is the magnitude of misorientation between the orientation of a spatial intragranular point i ( $g_i$ ) and the average orientation in the grain ( $g_{avg}$ ), following Pokharel et al. (2014). Together with the intragranular rotation map, dislocation densities in major active slip systems at a strain of 0.4 are displayed in Fig. 16d. Though the Schmid factor on the  $\{110\}$  slip systems (e.g. the slip system of B2) is initially greater than on the  $\{112\}$  slip planes, the dislocation densities are found to develop well on both  $\{110\}$  and  $\{112\}$  planes, due to the remarkable spatial variation in rotation inside the grain; i.e., at a strain of 0.4 (Fig. 16c), the contour for local orientation in the grain A is widely located throughout the regions where the Schmid factors are strong on both  $\{110\}$  and  $\{112\}$  slip planes.

Then, a grain B initially oriented in the [561] was selected since the initial orientation in the standard triangle has the maximum Schmid factor on the {112} planes (Fig. 17a). As shown in Fig. 17b, the grain tends to rotate toward the [111] direction such that the Schmid factor decreases along the corresponding great circle. Moreover, once again a significant spatial variation in rotation is observed again in the grain B at increasing strains of 0.2 and 0.4, as displayed in Fig. 17c. Dislocation densities in major active slip systems at a strain of 0.4 are also shown in Fig. 17d. The dislocation density is found to grow remarkably, especially for a slip system on the {112} plane (here, C2). This is quite reasonable since the contour for local orientation in the grain B is still located in the region where the maximum Schmid factor is incurred in the slip systems on the {112} planes.

Lastly, Fig. 18 shows the intragranular behavior of a grain C initially oriented in the [11  $\bar{9}8$ ] direction. The grain C was selected since it was closely aligned to [1 $\bar{1}1$ ] direction (Fig. 18a). It rotates much less than the other two grains presented in Figs. 16 and 17. Furthermore, as shown in Figs. 18b and 18c, there is no significant intragranular misorientation. Dislocation densities in the grain C grow very similarly to those in a single crystal loaded in the [1 $\bar{1}1$ ] direction, attributed to the small rotation during deformation. As shown in Fig. 18d, the dislocation densities in the grain C grow remarkably in the slip systems of A8, B12 and C10 that exhibit the highest Schmid factors in a single crystal loaded in the [1 $\bar{1}1$ ] direction.

# 4. Discussion

Plastic deformation in bcc tantalum has been deemed a complex process which involves diverse physical mechanisms across length-scales. In past decades, continuum mechanics-based crystal plasticity theories have been proposed to address the salient features of the rate- and temperature-dependent deformation in this important refractory metallic material. Furthermore, the continuum crystal plasticity theories have enabled modeling of the large inelastic behavior of tantalum single crystals and polycrystals. In this work, we have extended the crystal plasticity model to elucidate the deformations of both single- and polycrystal

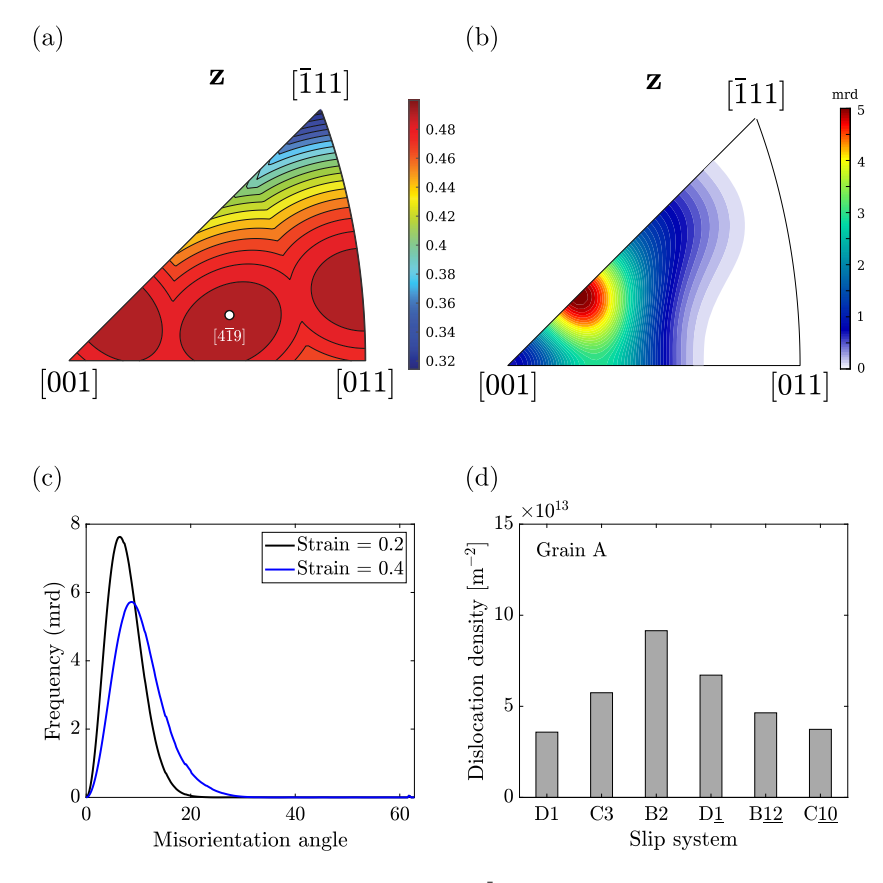


Fig. 16. Numerically predicted rotation and dislocation density in a grain A in the  $[4\bar{1}9]$  direction within the Voronoi-tessellated polycrystal domain. (a) Location of the  $[4\bar{1}9]$  direction on contour of the maximum Schmid factor, (b) countour of crystallographic orientations within the grain A at a strain of 0.4, (c) distribution of misorientation angle within the grain (strains of 0.2 and 0.4), (d) dislocation densities in slip systems on both {110} and {112} planes at a strain of 0.4.

tantalum materials at a wide range of strain rates and temperatures. Furthermore, using finite deformation constitutive modeling, experiments and numerical simulations, we have addressed the main features of deformation mechanisms, dislocation evolution, instability and the non-Schmid effects in bcc tantalum at both single- and polycrystal levels. Additionally, our work has been inspired by the recent mesoscopic studies on dislocation interactions throughout major slip systems on both {110} and {112} slip planes. The structurally unified modeling framework has been shown not only to reproduce the experimental data but also to provide critical insight into the plastic deformation mechanisms and microstructural evolutions at both single and polycrystal levels in bcc tantalum materials. Notably, most of the previous crystal plasticity-based modeling efforts have been focused on either single crystal behaviors (Lim et al., 2020; Nguyen et al., 2021) or polycrystal behaviors (Kothari and Anand, 1998; Bronkhorst et al., 2007; Lim et al., 2018) in these materials. However, in our unified modeling framework, the same constitutive model and parameters without any further modifications have been demonstrated to predict the single- and polycrystal behaviors simultaneously. Furthermore, by taking the dislocation microstructures and their interactions into account, our model well captured evolutions of textures and dislocation densities throughout polycrystalline network, which have not been explicitly represented in the previous isotropic polycrystal constitutive models including mechanical threshold stress (MTS) model (Follansbee and Kocks, 1988) and Zerilli–Armstrong model (Zerilli and Armstrong, 1987).

There are nevertheless some discrepancies between experimental data and our modeling results (e.g. tensile yield stress in the single crystal loaded in the [011] orientation at 77 K). As pointed out in Sections 2.2 and 2.3 on the single crystal behavior, the discrepancies are mainly attributed to the large variations in the single crystal data especially at high symmetric orientations available in the literature (Rittel et al., 2009; Whiteman et al., 2019; Lim et al., 2020; Nguyen et al., 2021). Notably, at low temperatures, yield stresses for tension and compression vary significantly among the literature (Byron, 1968; Sherwood et al., 1967; Hull et al., 1967), which implies the non-Schmid weighting factors may not be uniquely determined for this material. Moreover, as discussed in Stainier et al. (2002) and Lim et al. (2020), the ambiguity of the active slip systems in these materials at a range of strain rates and temperatures may lead to additional sources of discrepancies. Additionally, as noted in Cai et al. (2004), the kink nucleation barrier and its stress dependence can differ in the {112} planes and the {110} planes, from which Nguyen et al. (2021) showed that the orientation-dependent yield stresses can be better captured by employing the different values of the Peierls stress for each of the slip systems. Furthermore, in Nguyen et al. (2021), the Peierls stress was taken to be different in twinning

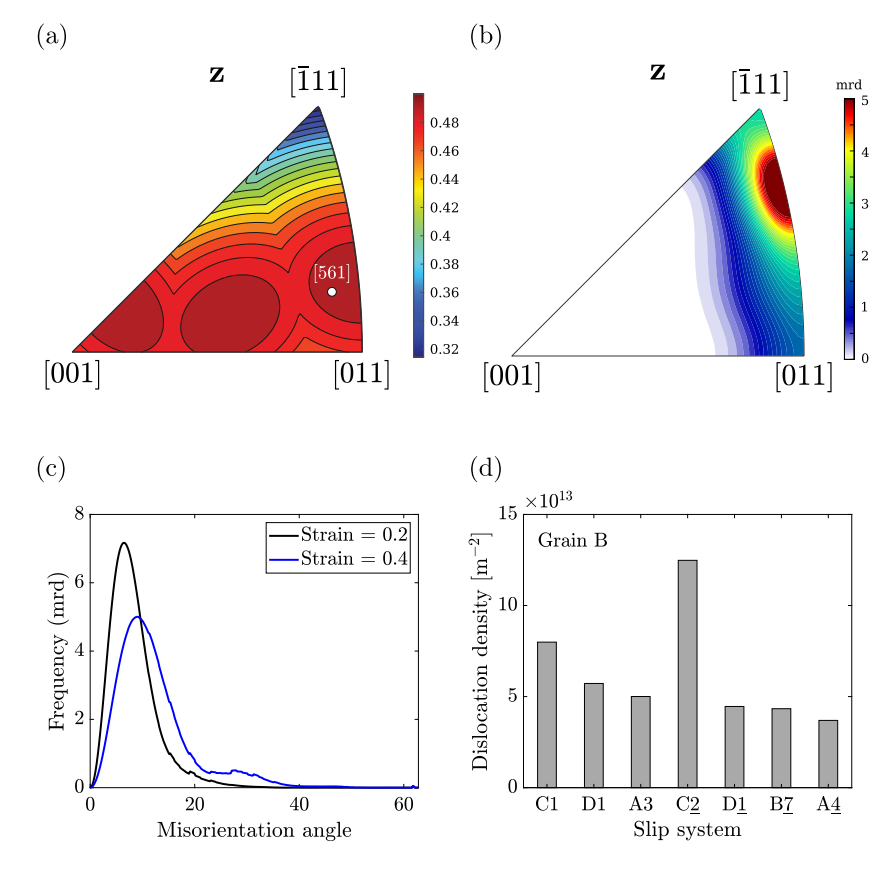


Fig. 17. Numerically predicted rotation and dislocation density in a grain B in the [561] direction within the Voronoi-tessellated polycrystal domain. (a) Location of the [561] direction on contour of the maximum Schmid factor, (b) countour of crystallographic orientations within the grain B at a strain of 0.4, (c) distribution of misorientation angle within the grain (strains of 0.2 and 0.4), (d) dislocation densities in slip systems on both {110} and {112} planes at a strain of 0.4.

and anti-twinning directions to better capture the non-Schmid effects especially on the {112} planes. Despite all their extensive parametric studies, there are still significant discrepancies between the single crystal data and modeling results. This implies that much needs to be done for further refinement of the single crystal plasticity theory for bcc materials involving active slip systems, multiple slip modes and their connections to the non-Schmid effects; especially in high symmetric orientations across a range of strain rates and temperatures.

Meanwhile, the non-convex nature of bcc single crystal plasticity discussed in Section 2.3.1 provides more physical insight into the deformation mechanisms in tantalum single crystals. As illustrated in Figs. 4–6, the solution to the simple boundary value problem associated with non-convex plastic potentials is not unique; there may not exist a unique solution that satisfies the minimum principle (Ortiz and Repetto, 1999; Ortiz et al., 2000). Possible non-convexity in dislocation density-based bcc single crystal plasticity models has been relatively unexplored and elusive since, in most of the previous models, the interaction characteristics throughout slip systems central to the evolution of dislocation densities as well as the associated hardening behavior have been too simplified for many bcc materials (e.g., Knezevic et al. (2014), Lim et al. (2015, 2020), Nguyen et al. (2021)). It should also be noted that many previous studies on non-convexity in crystal plasticity have been devoted to close-packed materials mainly with phenomenological hardening laws (Ortiz and Stainier, 1999; Stainier et al., 2002), for which nonlinear optimization methods were developed to determine slip activity and slip rate that minimize the incremental work density. Also, as recently recognized in Petryk and Kursa (2013, 2022), Petryk (2020), the non-convex plastic potential due to strong latent hardening is associated with active slip selection problems in rate-independent crystal plasticity in high symmetry orientations. Furthermore, non-convexity in crystal plasticity is strongly associated with the formation of microstructures that minimize the associated incremental energy (Ortiz et al., 2000; Hansen et al., 2010; Kochmann and Hackl, 2011; Yalçinkaya et al., 2012; Vidyasagar et al., 2018); all of these issues on rate-dependent and -independent, non-convex crystal plasticity still remain open questions in bcc materials.

Though our model captures many important aspects of plastic deformation in bcc tantalum, much needs to be done for further refinement of the theory for bcc materials. In particular, the model as proposed is structural only and therefore does not yet account for the proper partition of energy into the evolution of dislocation structure or thermal energy. This is particularly important for the ability of predicting the evolution of dislocation density and structure and properly accounting for the evolution of temperature within a thermally sensitive theory.

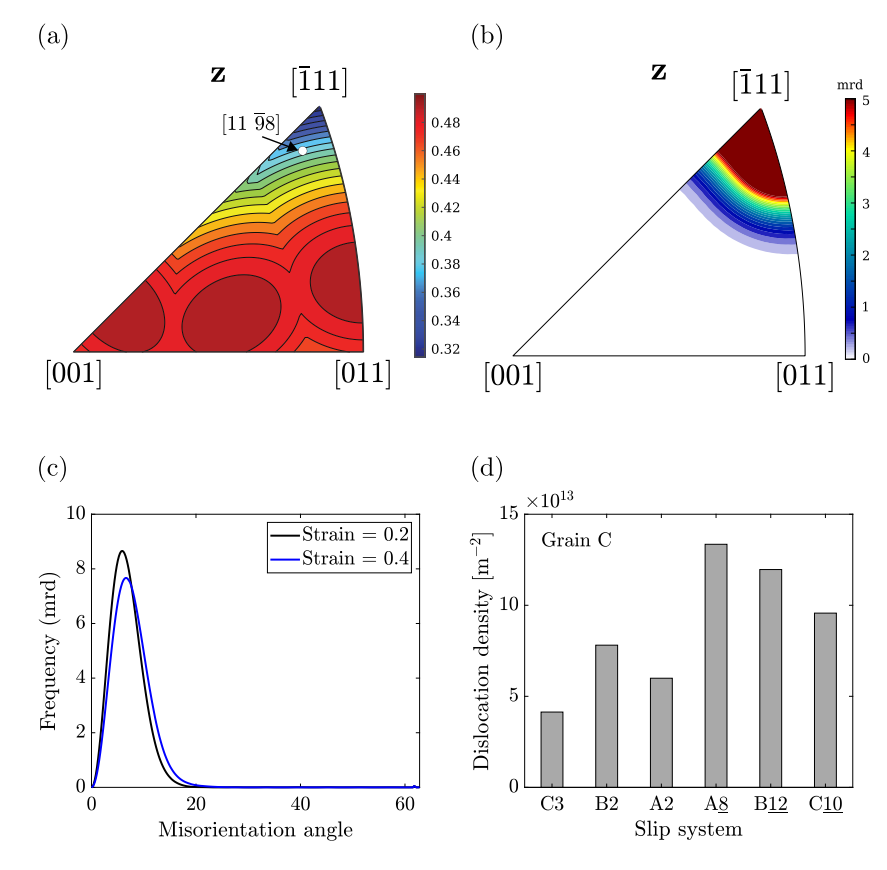


Fig. 18. Numerically predicted rotation and dislocation density in a grain C in the [11 98] direction within the Voronoi-tessellated polycrystal domain. (a) Location of the [11 98] direction on contour of the maximum Schmid factor, (b) countour of crystallographic orientations within the grain C at a strain of 0.4, (c) distribution of misorientation angle within the grain (strains of 0.2 and 0.4), (d) dislocation densities in slip systems on both {110} and {112} planes at a strain of 0.4

Furthermore, there is much we do not yet know about the mechanics and thermodynamics of bcc dislocation behavior and interaction within the potential kink-pair mechanisms of dislocation motion, particularly for the rate limiting screw dislocations and the role which edge dislocations play (Butler et al., 2018). These questions also certainly extend to defining the evolution of the structural and thermodynamic state of dislocations within metallic materials (e.g., Acharya (2010), Anand et al. (2015), Arora and Acharya (2020), Berdichevsky (2006, 2017, 2018b,a, 2019a,b), Chowdhury and Roy (2019), Hochrainer (2016), Jafari et al. (2017), Jiang et al. (2019), Langer et al. (2010), Langer (2015), Le (2018, 2019), Le et al. (2021), Levitas and Javanbakht (2015), Nieto-Fuentes et al. (2018), Po et al. (2019), Roy and Acharya (2005, 2006), Rivera-Díaz-del-Castillo and Huang (2012), Shizawa et al. (2001)). The open questions in bcc materials involving non-convexity, non-Schmid effects, dislocation interactions and their thermodynamic foundations should be revisited to improve the predictive capabilities of bcc single and polycrystal modeling framework.

#### 5. Conclusion

In this work, we have presented a unified framework for single- and polycrystal behaviors in bcc tantalum materials. At the single crystal level, we extended the finite deformation single crystal viscoplasticity model to account for the evolution and interaction of dislocations throughout the slip systems on both  $\{110\}$  and  $\{112\}$  planes. The single crystal model takes into account the dislocation interaction strengths critically associated with the hardening behavior as well as the microstructural evolution in bcc single crystals, informed by the recent dislocation dynamics simulation results for tantalum. The single crystal model with material parameters simply calibrated with experimental data on single crystal tantalum has been shown to accurately capture the major features in the stress–strain responses at low to high strain rates and at low to high temperatures in the major crystallographic orientations of [001],  $[01\bar{1}]$ , [111] and  $[\bar{1}49]$ . Furthermore, using the single crystal model, we addressed the effects of collinear interactions on slip activity and instability in multi-slip situations in single crystals loaded in high symmetry orientations. Non-convexity in the incremental plastic potential attributed to the strong collinear interactions was found to give rise to instability and bifurcation in the slip activity throughout the equivalent slip systems.

We then extend the dislocation density-based single crystal model to capture the non-Schmid effect at low temperature where slip on the  $\{110\}$  planes are more likely to be activated. Specifically, the extended model was found to accurately predict the tension-compression asymmetry in the single crystals loaded in high symmetry orientations, [001] and  $[01\bar{1}]$ . The possible non-convexity issues in these multi-slip situations was again resolved by introducing random misorientations throughout single crystals in our numerical simulations.

The single crystal model has been further underpinned by the successful representation of polycrystal behaviors in both experiments and numerical simulations. We conducted mechanical testing of polycrystal tantalum specimens together with ex situ neutron diffraction measurements for crystallographic textures and dislocation density at increasing strains. Numerical simulation results showed predictive capabilities of our modeling framework for the macroscopic stress-strain behavior and the corresponding crystallographic texturing at low to high strain rates and at low to high temperatures. The polycrystal model was also shown to be capable of reproducing the Taylor relation in which the flow stress is linearly proportional to the square root of the dislocation density experimentally evidenced in our ex situ neutron diffraction measurements on dislocation density growth in the polycrystal specimen at increasing strains. Furthermore, we have investigated spatial variations of rotation and dislocation density throughout the more realistic polycrystal network using numerical simulations on a Voronoi-tessellation-based polycrystal network. The numerically predicted local variations of the inelastic features provided insight into the underlying physical pictures for microstructural evolution within the individual crystals undergoing severe plastic deformation which recently have received great attention for polycrystal materials (Pokharel et al., 2014; Lieberman et al., 2016; Millett et al., 2020; Charpagne et al., 2021; Bhattacharyya et al., 2021). Indeed, the bcc crystal plasticity theory needs to be further extended to account for the influence of grain boundaries and thereby grain size effect that critically influence the characteristics of dislocation motion in and out of grains of a polycrystal, consequently culminating in substantial change in the macroscopic inelastic features. In addition, short- or long-range spatial interactions between dislocations and grain boundaries or between different grains throughout the polycrystal network should be taken into account for accurately modeling extreme events such as damage nucleation and growth. Towards this end, more realistic, grain boundary conforming polycrystal models must be established using the electron backscatter diffraction and state-of-the-art measurement techniques for the actual microstructures for bcc materials (Foster et al., 2021).

#### Declaration of competing interest

The authors declare the following financial interests/personal relationships which may be considered as potential competing interests: Hansohl Cho reports financial support was provided by National Research Foundation of Korea. Curt Bronkhorst reports financial support was provided by National Science Foundation.

#### Acknowledgments

This work was funded by National Research Foundation (NRF) of Korea (Grant No. 2020R1C1C101324813 and 2021R1A4A103278312) and National Science Foundation (NSF), United States CMMI (Grant No. 2118399). This work has also benefitted from the use of the Los Alamos Neutron Science Center (LANSCE) at Los Alamos National Laboratory. Los Alamos National Laboratory is operated by Triad National Security, LLC, for the National Nuclear Security Administration of the U.S. Department of Energy under contract number 89233218NCA000001.

# Appendix A. Time integration procedure for single crystal model

The implicit time integration procedure we have used in this work is summarized, as follows. Let  $\tau = t + \Delta t$ . Using the given,

- 1. F(t),  $F(\tau)$ ,
- 2.  $\mathbf{F}^{\mathbf{p}}(t)$ ,  $s^{\alpha}(t)$ ,  $\mathbf{T}(t)$

our task is to update  $\{\mathbf{F}^p(\tau), s^{\alpha}(\tau), \rho^{\alpha}(\tau) \text{ and } \mathbf{T}(\tau)\}.$ 

Components of the fourth-order elasticity tensor in the global basis are calculated by,

$$C_{ijkl} = Q_{ip}Q_{jq}Q_{kr}Q_{ls}C_{pars}^{c}, \tag{A.1}$$

where  $C_{pqrs}^c$  is the component of the fourth-order elasticity tensor in the crystal basis and **Q** is the orthogonal tensor which rotates the crystal basis to the global basis (e.g. Kalidindi et al. (1992)). Trial quantities are then calculated by,

$$\mathbf{F}_{tr}^{e} = \mathbf{F}(\tau)\mathbf{F}^{p-1}(t),\tag{A.2}$$

$$\mathbf{C}_{\mathrm{tr}}^{\mathrm{e}} = \mathbf{F}_{\mathrm{tr}}^{\mathrm{eT}} \mathbf{F}_{\mathrm{tr}}^{\mathrm{e}},\tag{A.3}$$

$$\mathbf{E}_{\text{tr}}^{\text{e}} = \frac{1}{2}(\mathbf{C}_{\text{tr}}^{\text{e}} - \mathbf{1}),$$
 (A.4)

$$\mathbf{T}_{\text{tr}}^{\text{e}} = C\left[\mathbf{E}_{\text{tr}}^{\text{e}} - \mathbf{A}(\theta - \theta_0)\right],\tag{A.5}$$

$$\mathbf{B}^{\alpha} = \operatorname{symm}[\mathbf{C}_{\operatorname{tr}}^{\operatorname{e}} \mathbb{S}_{0}^{\alpha}], \tag{A.6}$$

$$\mathbf{C}^{a} = C \left[ \mathbf{B}^{a} \right]. \tag{A.7}$$

The following coupled implicit equations for  $\mathbf{T}^{\mathbf{e}}(\tau)$ ,  $s^{\alpha}(\tau)$  and  $\rho^{\alpha}(\tau)$ ,

$$\mathbf{T}^{\mathbf{e}}(\tau) = \mathbf{T}_{\mathrm{tr}}^{\mathbf{e}} - \sum_{\alpha=1}^{N} \Delta \gamma_{\mathbf{p}}^{\alpha} \left( \mathbf{T}^{\mathbf{e}}(\tau), \, s^{\alpha}(\tau) \right) \mathbf{C}^{\alpha}, \tag{A.8}$$

$$s^{\alpha}(\tau) = s^{\alpha}(t) + \Delta s^{\alpha} \left( \Delta \gamma_{\mathbf{p}}^{\beta} \left( \mathbf{T}^{\mathbf{e}}(\tau), s^{\beta}(\tau) \right), \rho^{\beta}(\tau) \right), \tag{A.9}$$

$$\rho^{\alpha}(\tau) = \rho^{\alpha}(t) + \Delta \rho^{\alpha} \left( \Delta \gamma_{n}^{\alpha} \left( \mathbf{T}^{e}(\tau), s^{\alpha}(\tau) \right), \rho^{\beta}(\tau) \right), \tag{A.10}$$

with,

$$\Delta \gamma_{\rm p}^{\alpha} = \Delta t \, \dot{\gamma_0} \exp \left( -\frac{\Delta G}{k_B \theta} \left\langle 1 - \left( \frac{|\tau^{\alpha}| - s^{\alpha}(\tau)}{\widetilde{s_l}} \right)^p \right\rangle^q \right); \quad \text{where } \tau^{\alpha} = \mathbf{T}^{\rm e}(\tau) \, : \, \mathbb{S}_0^{\alpha}, \tag{A.11}$$

 $\Delta s^{\alpha} = \Delta t \, \dot{s}^{\alpha} (\tau)$ 

$$= \frac{1}{2} \mu \frac{\sum_{\beta} a^{\alpha\beta}}{\sqrt{\sum_{\beta} a^{\alpha\beta} \rho^{\beta}(\tau)}} \left( \sqrt{\sum_{\gamma} d^{\beta\gamma} \rho^{\gamma}(\tau)} - 2y_{c}^{\beta} \rho^{\beta}(\tau) \right) \left| \Delta y_{p}^{\beta} \left( \mathbf{T}^{e}(\tau), s^{\beta}(\tau) \right) \right|, \tag{A.12}$$

$$\Delta \rho^{\alpha} = \Delta t \, \dot{\rho}^{\alpha}(\tau) = \frac{1}{b} \left( \sqrt{\sum_{\beta} d^{\alpha\beta} \rho^{\beta}(\tau)} - 2y_{c}^{\alpha} \rho^{\alpha}(\tau) \right) |\Delta \gamma_{p}^{\alpha} \left( \mathbf{T}^{e}(\tau), \, s^{\alpha}(\tau) \right)|, \tag{A.13}$$

where

$$y_c^{\alpha} = y_{c0} \left( 1 - \frac{k_B \theta}{A_{rec}} \ln \left| \frac{\Delta \gamma_p^{\alpha}}{\Delta t \, \dot{\gamma}_0} \right| \right), \tag{A.14}$$

are solved using the following two-step iteration procedure.

First, the elastic 2nd Piola stress is updated, keeping  $s^{\alpha}(\tau)$  and  $\rho^{\alpha}(\tau)$  fixed, by,

$$\mathbf{T}_{n+1}^{e}(\tau) = \mathbf{T}_{n}^{e}(\tau) - \mathcal{J}_{n}^{-1}[\mathbf{G}_{n}],$$
 (A.15)

$$\mathbf{G}_{\mathbf{n}} \equiv \mathbf{T}_{n}^{\mathbf{e}}(\tau) - \mathbf{T}_{\mathrm{tr}}^{\mathbf{e}} + \sum_{\alpha=1}^{N} \Delta \gamma_{\mathbf{p}}^{\alpha} \left( \mathbf{T}_{n}^{\mathbf{e}}(\tau), \, s_{k}^{\alpha}(\tau) \right) \mathbf{C}^{\alpha}, \tag{A.16}$$

$$\mathcal{J}_{n} \equiv \mathcal{I} + \sum_{\alpha=1}^{N} \mathbf{C}^{\alpha} \otimes \frac{\partial}{\partial \mathbf{T}_{n}^{\mathbf{e}}(\tau)} \Delta \gamma_{\mathbf{p}}^{\alpha} \left( \mathbf{T}_{n}^{\mathbf{e}}(\tau), s_{k}^{\alpha}(\tau) \right), \tag{A.17}$$

where  $\mathcal{I}$  is the fourth-order identity tensor. The elastic 2nd Piola stress is accepted if,

$$\left| \left[ \mathcal{J}_n^{-1}[\mathbf{G}_n] \right]_{ii} \right| < \Delta T_{\text{tol}}^{\text{e}}, \tag{A.18}$$

where  $\Delta T_{\rm tol}^{\rm e}$  is the tolerance for stress. The Newton correction in Eq. (A.15) is accepted if,

$$\max_{\alpha} |\Delta \gamma_{\mathsf{p}}^{\alpha} \left( \mathbf{T}_{n+1}^{\mathsf{e}}(\tau), \, s_{k}^{\alpha}(\tau) \right)| < \Delta \gamma_{\mathsf{p}, \, \mathsf{tol}}, \tag{A.19}$$

where  $\Delta \gamma_{p, tol}$  is the upper bound for the incremental shear strain rate. Here, we have used  $\Delta \gamma_{p, tol} = 0.5$ . However, if the constraint in Eq. (A.19) is not satisfied, the elastic stress ( $T_{n+1}^e$ ) is further corrected by,

$$[T_{n+1}^{e}(\tau)]_{ij} = [T_{n}^{e}(\tau)]_{ij} + \eta \Delta T_{ij}^{e}, \tag{A.20}$$

where  $\Delta T^e = -\mathcal{J}_n^{-1}[G_n]$  and  $\eta$  is the correction factor. Here, we have used  $\eta = 0.25$ . This correction is repeated until the corrected elastic stress satisfies the constraint.

Using the converged  $T^e(\tau)$ , the slip resistance ( $s^{\alpha}(\tau)$ ) and the dislocation density ( $\rho^{\alpha}(\tau)$ ) are simply updated with no iterations by,

$$s_{k+1}^{\alpha}(\tau) = s^{\alpha}(t) + \Delta s^{\alpha} \left( \Delta \gamma_{\mathbf{p}}^{\beta} \left( \mathbf{T}_{n+1}^{\mathbf{e}}(\tau), s_{k}^{\beta}(\tau) \right), \rho_{k}^{\beta} \right)$$

$$= s^{\alpha}(t) + \frac{1}{2} \mu \frac{\sum_{\beta} a^{\alpha\beta}}{\sqrt{\sum_{c} a^{\alpha\beta} \rho_{k}^{\beta}}} \left( \sqrt{\sum_{\gamma} d^{\beta\gamma} \rho_{k}^{\gamma}} - 2 y_{c}^{\beta} \rho_{k}^{\beta} \right) \left| \Delta \gamma_{\mathbf{p}}^{\beta} \left( \mathbf{T}_{n+1}^{\mathbf{e}}(\tau), s_{k}^{\beta}(\tau) \right) \right|, \tag{A.21}$$

and

$$\rho_{k+1}^{\alpha}(\tau) = \rho^{\alpha}(t) + \Delta \rho^{\alpha} \left( \Delta \gamma_{\mathbf{p}}^{\alpha} \left( \mathbf{T}_{n+1}^{\mathbf{e}}(\tau), s_{k}^{\alpha}(\tau) \right), \rho_{k}^{\beta} \right)$$

$$= \rho^{\alpha}(t) + \frac{1}{b} \left( \sqrt{\sum_{\beta} d^{\alpha\beta} \rho_{k}^{\beta}} - 2 y_{c}^{\alpha} \rho_{k}^{\alpha} \right) \left| \Delta \gamma_{\mathbf{p}}^{\alpha} \left( \mathbf{T}_{n+1}^{\mathbf{e}}(\tau), s_{k}^{\beta}(\tau) \right) \right|. \tag{A.22}$$

The slip resistance is accepted if,

$$\max|s_{k+1}^{\alpha} - s_k^{\alpha}| < s_{\text{tol}}^{\alpha}. \tag{A.23}$$

If not accepted, we go back to the first level of the iteration procedure in Eq. (A.15) upon using the updated values,  $s_{k+1}^{\alpha}$  and  $\rho_{k+1}^{\alpha}$ . Once  $\mathbf{T}^{\mathbf{e}}(\tau)$ ,  $s^{\alpha}(\tau)$ ,  $\rho^{\alpha}(\tau)$  in the two-step iteration procedure are accepted, the kinematic variables are then updated. The Cauchy stress and the temperature at the end of the increment are then updated by Eqs. (14) and (22), respectively.

#### Appendix B. Computation of material Jacobian

The implicit finite element procedure employed in this work uses a Newton-type iteration which requires a fourth-order tangent also known as Jacobian at the end of the increment defined by,

$$W(\tau) \equiv \frac{\partial \mathbf{T}(\tau)}{\partial \mathbf{E}_{\ell}(\tau)},\tag{B.1}$$

where  $T(\tau)$  is the Cauchy stress and  $E_{\tau}(\tau)$  is the symmetric relative strain tensor.<sup>2</sup> The Cauchy stress is calculated by,

$$\mathbf{T}(\tau) = \frac{1}{\det \mathbf{F}^{\mathbf{e}}(\tau)} [\mathbf{F}^{\mathbf{e}}(\tau)\mathbf{T}^{\mathbf{e}}(\tau)\mathbf{F}^{\mathbf{e}T}(\tau)]. \tag{B.2}$$

From Eq. (B.2) we have,

$$d\mathbf{T} = \frac{1}{\det \mathbf{F}^e} [d\mathbf{F}^e \mathbf{T}^e \mathbf{F}^{eT} + \mathbf{F}^e d\mathbf{T}^e \mathbf{F}^{eT} + \mathbf{F}^e \mathbf{T}^e d\mathbf{F}^{eT} - (\mathbf{F}^e \mathbf{T}^e \mathbf{F}^{eT}) \operatorname{tr}(d\mathbf{F}^e \mathbf{F}^{e-1})]. \tag{B.3}$$

Hence, the tangent tensor is expressed as,

$$W_{ijkl} = \frac{1}{\det \mathbf{F}^{e}} [S_{imkl} T_{mn}^{e} F_{nj}^{eT} + F_{im}^{e} Q_{mnkl} F_{nj}^{eT} + F_{im}^{e} T_{mn}^{e} S_{jnkl} - F_{im}^{e} T_{mn}^{e} F_{nj}^{eT} S_{pqkl} F_{qp}^{e-1}],$$
(B.4)

with

$$S \equiv \frac{\partial \mathbf{F}^{e}}{\partial \mathbf{E}_{t}}$$
 and  $Q \equiv \frac{\partial \mathbf{T}^{e}}{\partial \mathbf{E}_{t}}$ . (B.5)

Since the relative stretch is small in this work,

$$\mathbf{E}_{t} = \ln \mathbf{U}_{t} \approx \mathbf{U}_{t} - \mathbf{1},\tag{B.6}$$

Where  $\mathbf{U}_t$  is the relative stretch tensor. Therefore,  $d\mathbf{E}_t \approx d\mathbf{U}_t$  and the fourth-order tensor S and Q is expressed by,

$$S = \frac{\partial F^e}{\partial U_e}$$
 and  $Q = \frac{\partial T^e}{\partial U_e}$ . (B.7)

(1) Calculation of S

The elastic deformation gradient at  $\tau$  can be obtained by,

$$\mathbf{F}^{\mathbf{e}}(\tau) = \mathbf{F}(\tau)\mathbf{F}^{\mathbf{p}-1}(\tau) = \mathbf{R}_{t}\mathbf{U}_{t}\mathbf{F}^{\mathbf{e}}(t)\left\{\mathbf{1} - \sum_{\alpha=1}^{N} \Delta \gamma_{\mathbf{p}}{}^{\alpha}\mathbb{S}_{0}^{\alpha}\right\}. \tag{B.8}$$

Then,

$$S_{ijkl} = \frac{\partial F_{ij}^{e}}{\partial U_{(t)kl}} = \frac{\partial}{\partial U_{(t)kl}} \left[ R_{(t)im} U_{(t)mn} F_{np}^{e}(t) \left\{ \delta_{pj} - \sum_{\alpha=1}^{N} \Delta \gamma_{p}^{\alpha} \mathbb{S}_{0 pj}^{\alpha} \right\} \right]$$

$$= R_{(t)ik} F_{lj}^{e}(t) - R_{(t)ik} F_{lp}^{e}(t) \sum_{\alpha=1}^{N} \Delta \gamma_{p}^{\alpha} \mathbb{S}_{0 pj}^{\alpha} - R_{(t)im} U_{(t)mn} F_{np}^{e}(t) \sum_{\alpha=1}^{N} \mathcal{R}_{kl}^{\alpha} \mathbb{S}_{0 pj}^{\alpha},$$
(B.9)

with  $\mathcal{R}^{\alpha} = \frac{\partial \Delta \gamma_p^{\ \alpha}}{\partial U_t}$ , and subscript (t) denotes relative quantities. (2) Calculation of Q

From Eq. (A.8)

$$Q_{ijkl} = \frac{\partial T_{ij}^{e}}{\partial U_{(t)kl}} = D_{ijkl} - \sum_{\alpha=1}^{N} \mathcal{R}_{kl}^{\alpha} C_{ij}^{\alpha} - \sum_{\alpha=1}^{N} \Delta \gamma_{p}^{\alpha} \mathcal{J}_{ijkl}^{\alpha}, \tag{B.10}$$

where  $\mathcal{D} = \frac{\partial T_{tr}^{t}}{\partial L}$  and  $\mathcal{J}^{\alpha} = \frac{\partial C^{\alpha}}{\partial L}$ .  $\mathcal{D}$  is expressed by,

$$D_{ijkl} = \frac{\partial T_{(tr)ij}^{e}}{\partial U_{(t)kl}} = \frac{1}{2} C_{ijmn} \mathcal{L}_{mnkl}. \tag{B.11}$$

<sup>&</sup>lt;sup>2</sup> The relative deformation gradient is defined as  $\mathbf{F}_{t}(\tau) = \mathbf{F}(\tau)\mathbf{F}^{-1}(t)$ . Similar to the deformation gradient, the relative deformation gradient tensor also allows for the polar decomposition,  $\mathbf{F}_t(\tau) = \mathbf{R}_t(\tau)\mathbf{U}_t(\tau)$  where  $\mathbf{R}_t$  is relative rotation tensor and  $\mathbf{U}_t$  is relative stretch tensor. The relative strain tensor is then defined as  $\mathbf{E}_{t}(\tau) = \ln \mathbf{U}_{t}(\tau).$ 

And  $\mathcal{L}$  is calculated by,

$$\mathcal{L}_{ijkl} = \frac{\partial C_{(\text{tr})ij}^{e}}{\partial U_{(t)kl}} = \frac{\partial}{\partial U_{(t)kl}} \left[ F_{mi}^{p-1}(t) F_{nm}(\tau) F_{np}(\tau) F_{pj}^{p-1}(t) \right] \\
= \frac{\partial}{\partial U_{(t)kl}} \left[ F_{mi}^{e}(t) U_{(t)mn}(\tau) U_{(t)np}(\tau) F_{pj}^{e}(t) \right] \\
= F_{mi}^{e}(t) \delta_{mk} \delta_{nl} U_{(t)np} F_{pj}^{e}(t) + F_{mi}^{e}(t) U_{(t)mn} \delta_{nk} \delta_{pl} F_{pj}^{e}(t) \\
= F_{ej}^{e}(t) U_{(t)lp} F_{ni}^{e}(t) + F_{mi}^{e}(t) U_{(t)mk} F_{pj}^{e}(t). \tag{B.12}$$

Furthermore, from Eqs. (A.6) and (A.7),  $\mathcal{J}^{\alpha}$  is calculated by,

$$J_{ijkl}^{\alpha} = \frac{\partial C_{ij}^{\alpha}}{\partial U_{(t)kl}} = \frac{\partial}{\partial U_{(t)kl}} \left[ \frac{1}{2} C_{ijmn} \left( C_{(tr)mp} \mathbb{S}_{0pn}^{\alpha} + \mathbb{S}_{0pm}^{\alpha} C_{(tr)pn} \right) \right]$$

$$= \frac{1}{2} \left[ C_{ijmn} \mathcal{L}_{mpkl} \mathbb{S}_{0pn}^{\alpha} + C_{ijmn} \mathbb{S}_{0pm}^{\alpha} \mathcal{L}_{pnkl} \right]. \tag{B.13}$$

Moreover,  $\mathcal{R}^{\alpha}$  is calculated by,

$$\mathcal{R}_{ij}^{\alpha} = \frac{\partial \Delta \gamma_{\mathbf{p}}^{\alpha}(\mathbf{T}^{e})}{\partial U_{(t)ij}} = \frac{\partial \Delta \gamma_{\mathbf{p}}^{\alpha}(\mathbf{T}^{e})}{\partial T_{kl}^{e}} \frac{\partial T_{kl}^{e}}{\partial U_{(t)ij}} = \mathcal{B}_{kl}^{\alpha} \mathcal{Q}_{klij}, \tag{B.14}$$

with

$$\mathcal{B}_{ij}^{\alpha} = \frac{\partial \Delta \gamma_{\mathbf{p}}^{\alpha}}{\partial T_{ij}^{e}} = \frac{\partial \Delta \gamma_{\mathbf{p}}^{\alpha}}{\partial \tau^{\alpha}} \frac{\partial \tau^{\alpha}}{\partial T_{ij}^{e}} = \frac{\partial \Delta \gamma_{\mathbf{p}}^{\alpha}}{\partial \tau^{\alpha}} \frac{1}{2} (\mathbb{S}_{0ij}^{\alpha} + \mathbb{S}_{0ji}^{\alpha}). \tag{B.15}$$

Q is therefore expressed by,

$$Q = D - \sum_{\alpha=1}^{N} (\mathbf{C}^{\alpha} \otimes \mathcal{B}^{\alpha}) Q - \sum_{\alpha=1}^{N} \Delta \gamma_{\mathbf{p}}{}^{\alpha} \mathcal{J}^{\alpha}.$$
(B.16)

Then, rearranging Eq. (B.16), we have,

$$Q = \left[ \mathbf{I} + \sum_{\alpha=1}^{N} (\mathbf{C}^{\alpha} \otimes \mathbf{B}^{\alpha}) \right]^{-1} \left[ \mathbf{D} - \sum_{\alpha=1}^{N} \Delta \gamma_{\mathbf{p}}^{\alpha} \mathbf{J}^{\alpha} \right], \tag{B.17}$$

$$\mathcal{K} \equiv \mathcal{I} + \sum_{\alpha=1}^{N} (\mathbf{C}^{\alpha} \otimes \mathcal{B}^{\alpha}), \tag{B.18}$$

$$\mathcal{M} \equiv \mathcal{D} - \sum_{i=1}^{N} \Delta \gamma_{\mathbf{p}}^{\alpha} \mathcal{J}^{\alpha}. \tag{B.19}$$

The computation of the tangent is summarized as follows,

- 1.  $\mathbf{U}_t = \mathbf{R}_t^{-1} \mathbf{F}(\tau) \mathbf{F}^{-1}(t)$ ,
- 2.  $C_{ijkl} = Q_{ip}Q_{jq}Q_{kr}Q_{ls}C_{pars}^c$ ,
- 3.  $\mathcal{L}_{ijkl} = F_{ki}^e(t)U_{(t)lp}F_{ni}^e(t) + F_{mi}^e(t)U_{(t)mk}F_{li}^e(t)$ ,
- 4.  $D_{ijkl} = \frac{1}{2}C_{ijmn}\mathcal{L}_{mnkl}$ ,
- 5.  $J_{ijkl}^{\alpha} = \frac{1}{2} \left[ C_{ijmn} \mathcal{L}_{mpkl} \mathbb{S}_{0 pn}^{\alpha} + C_{ijmn} \mathbb{S}_{0 pm}^{\alpha} \mathcal{L}_{pnkl} \right],$ 6.  $B_{ij}^{\alpha} = \frac{\partial \Delta y_{p}^{h}}{\partial \tau^{\alpha}} \frac{1}{2} (\mathbb{S}_{0 ij}^{\alpha} + \mathbb{S}_{0 ji}^{\alpha}),$
- 7.  $\mathcal{K}_{ijkl} = \delta_{ik}\delta_{jl} + \sum_{\alpha=1}^{N} C_{ij}^{\alpha} \mathcal{B}_{kl}^{\alpha}$ , (Calculated in reduced form  $\mathcal{K}_{IJ}$ )
- 8.  $\mathcal{M}_{ijkl} = \mathcal{D}_{ijkl} \sum_{\alpha=1}^{N} \Delta \gamma_{\mathbf{p}}^{\alpha} \mathcal{J}_{ijkl}^{\alpha}$ . (Calculated in reduced form  $\mathcal{M}_{IJ}$ )
- 9.  $Q_{ijkl} = \mathcal{K}_{ijmn}^{-1} \mathcal{M}_{mnkl}$  (Calculated in reduced form  $Q_{IJ}$ )
- 10.  $\mathcal{R}_{ii}^{\alpha} = \mathcal{B}_{kl}^{\alpha} \mathcal{Q}_{klij}$
- 11.  $S_{ijkl} = R_{(l)ik}F_{lj}^{e} R_{(l)ik}F_{lj}^{e} \sum_{\alpha=1}^{N} \Delta \gamma_{p}^{\alpha} \mathbb{S}_{0pj}^{\alpha} R_{(l)im}U_{(l)mn}F_{np}^{e} \sum_{\alpha=1}^{N} \mathcal{R}_{kl}^{\alpha} \mathbb{S}_{0pj}^{\alpha},$ 12.  $W_{ijkl} = \frac{1}{\det \mathbb{F}^{e}} [S_{imkl}T_{mn}^{e}F_{nj}^{eT} + F_{im}^{e}Q_{mnkl}F_{nj}^{eT} + F_{im}^{e}T_{mn}^{e}S_{jnkl} F_{im}^{e}T_{mn}^{e}F_{nj}^{eT}S_{pqkl}F_{qp}^{e-1}]$

# Appendix C. Stress-strain behavior with varying non-Schmid parameters

See Fig. 19.

# Appendix D. Supplementary data

Supplementary material related to this article can be found online at https://doi.org/10.1016/j.ijplas.2023.103529.

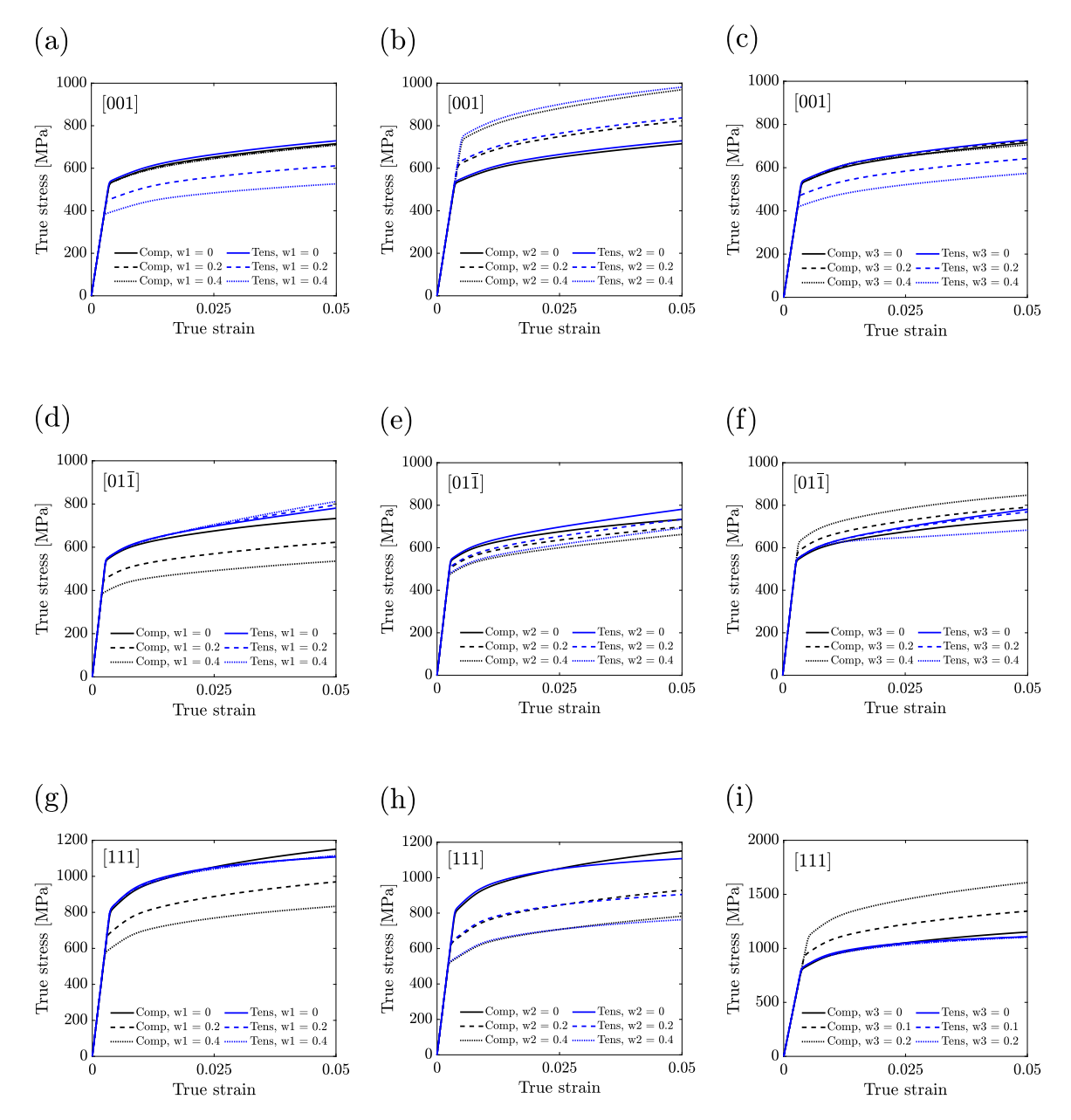


**Fig. 19.** Stress–strain behaviors of a bcc single crystal under uniaxial tension and compression with varying  $w_1$ ,  $w_2$  and  $w_3$  (strain rate:  $10^{-3}$  s<sup>-1</sup>, temperature: 77 K). (a)  $w_1$ , (b)  $w_2$ , (c)  $w_3$  in [001] orientation, (d)  $w_1$ , (e)  $w_2$ , (f)  $w_3$  in [01 $\overline{1}$ ] orientation, (g)  $w_1$ , (h)  $w_2$ , (i)  $w_3$  in [111] orientation.

# References

Acharya, A., 2010. New inroads in an old subject: Plasticity, from around the atomic to the macroscopic scale. J. Mech. Phys. Solids 58 (5), 766–778.

Anand, L., 2004. Single-crystal elasto-viscoplasticity: application to texture evolution in polycrystalline metals at large strains. Comput. Methods Appl. Mech. Eng. 193 (48–51), 5359–5383.

Anand, L., Gurtin, M.E., Reddy, B.D., 2015. The stored energy of cold work, thermal annealing, and other thermodynamic issues in single crystal plasticity at small length scales. Int. J. Plast. 64, 1–25.

Ardeljan, M., Beyerlein, I.J., Knezevic, M., 2014. A dislocation density based crystal plasticity finite element model: Application to a two-phase polycrystalline HCP/BCC composites. J. Mech. Phys. Solids 66, 16–31.

Arora, R., Acharya, A., 2020. Dislocation pattern formation in finite deformation crystal plasticity. Int. J. Solids Struct. 184, 114-135.

Asaro, R.J., 1983. Micromechanics of crystals and polycrystals. In: Hutchinson, J.W., Wu, T.Y. (Eds.), In: Advances in Applied Mechanics, vol. 23, Elsevier, pp. 1–115.

Asaro, R.J., Needleman, A., 1985. Overview no. 42 Texture development and strain hardening in rate dependent polycrystals. Acta Metall. 33 (6), 923–953. Bachmann, F., Hielscher, R., Schaeben, H., 2010. Texture analysis with MTEX- Free and open source software toolbox. Solid State Phenomena 160, 63–68.

Berdichevsky, V.L., 2006. On thermodynamics of crystal plasticity. Scr. Mater. 54 (5), 711-716.

Berdichevsky, V.L., 2017. A continuum theory of edge dislocations. J. Mech. Phys. Solids 106, 95-132.

Berdichevsky, V.L., 2018a. Entropy and temperature of microstructure in crystal plasticity. Internat. J. Engrg. Sci. 128, 24-30.

Berdichevsky, V.L., 2018b. Why is classical thermodynamics insufficient for solids? In: 2018 AIAA/ASCE/AHS/ASC Structures, Structural Dynamics, and Materials Conference. American Institute of Aeronautics and Astronautics.

Berdichevsky, V.L., 2019a. Beyond classical thermodynamics: Dislocation-mediated plasticity. J. Mech. Phys. Solids 129, 83-118.

Berdichevsky, V.L., 2019b. Dynamic equations for a periodic set of edge dislocations. Arch. Appl. Mech. 89, 425-436.

Berger, A., Witz, J.-F., El Bartali, A., Sadat, T., Limodin, N., Dubar, M., Najjar, D., 2022. Experimental investigation of early strain heterogeneities and localizations in polycrystalline *α* -Fe during monotonic loading. Int. J. Plast. 153, 103253.

Beyerlein, I.J., Tomé, C.N., 2008. A dislocation-based constitutive law for pure Zr including temperature effects. Int. J. Plast. 24 (5), 867-895.

Bhattacharyya, J.J., Nair, S., Pagan, D.C., Tari, V., Lebensohn, R.A., Rollett, A.D., Agnew, S.R., 2021. Elastoplastic transition in a metastable β-Titanium alloy, Timetal-18 – An in-situ synchrotron X-ray diffraction study. Int. J. Plast. 139, 102947.

Bienvenu, B., Dezerald, L., Rodney, D., Clouet, E., 2022. Ab initio informed yield criterion across body-centered cubic transition metals. Acta Mater. 236, 118098. Bronkhorst, C.A., Cerreta, E.K., Xue, Q., Maudlin, P.J., Mason, T.A., Gray, G.T., 2006. An experimental and numerical study of the localization behavior of tantalum and stainless steel. Int. J. Plast. 22 (7), 1304–1335.

Bronkhorst, C.A., Cho, H., Marcy, P.W., Vander Wiel, S.A., Gupta, S., Versino, D., Anghel, V., Gray, G.T., 2021. Local micro-mechanical stress conditions leading to pore nucleation during dynamic loading. Int. J. Plast. 137, 102903.

Bronkhorst, C.A., Gray, G.T., Addessio, F.L., Livescu, V., Bourne, N.K., McDonald, S.A., Withers, P.J., 2016. Response and representation of ductile damage under varying shock loading conditions in tantalum. J. Appl. Phys. 119 (8), 085103.

Bronkhorst, C.A., Hansen, B.L., Cerreta, E.K., Bingert, J.F., 2007. Modeling the microstructural evolution of metallic polycrystalline materials under localization conditions. J. Mech. Phys. Solids 55 (11), 2351–2383.

Bronkhorst, C.A., Kalidindi, S., Anand, L., 1992. Polycrystalline plasticity and the evolution of crystallographic texture in FCC metals. Philos. Trans. R. Soc. Lond. Ser. A Phys. Eng. Sci. 341 (1662), 443–477.

Bronkhorst, C.A., Mayeur, J.R., Livescu, V., Pokharel, R., Brown, D.W., Gray, G.T., 2019. Structural representation of additively manufactured 316L austenitic stainless steel. Int. J. Plast. 118, 70–86.

Brown, D.W., Okuniewski, M.A., Sisneros, T.A., Clausen, B., Moore, G.A., Balogh, L., 2016. Neutron diffraction measurement of residual stresses, dislocation density and texture in Zr-bonded U-10Mo "mini" fuel foils and plates. J. Nucl. Mater. 482, 63–74.

Butler, B.G., Paramore, J.D., Ligda, J.P., Ren, C., Fang, Z.Z., Middlemas, S.C., Hemker, K.J., 2018. Mechanisms of deformation and ductility in tungsten–A review. Int. J. Refractory Metals Hard Mater. 75, 248–261.

Byron, J.F., 1968. Plastic deformation of tantalum single crystals. II. The orientation dependence of yield. J. Less-Common Met. 14 (2), 201-210.

Cai, W., Bulatov, V.V., Chang, J., Li, J., Yip, S., 2004. Chapter 64 - dislocation core effects on mobility. In: Nabarro, F., Hirth, J. (Eds.), Dislocations in Solids. Vol. 12. Elsevier, pp. 1–80.

Cereceda, D., Diehl, M., Roters, F., Raabe, D., Perlado, J.M., Marian, J., 2016. Unraveling the temperature dependence of the yield strength in single-crystal Tungsten using atomistically-informed crystal plasticity calculations. Int. J. Plast. 78, 242–265.

Charpagne, M.A., Hestroffer, J.M., Polonsky, A.T., Echlin, M.P., Texier, D., Valle, V., Beyerlein, I.J., Pollock, T.M., Stinville, J.C., 2021. Slip localization in Inconel 718: A three-dimensional and statistical perspective. Acta Mater. 215, 117037.

Chen, S.R., Gray, G.T., 1996. Constitutive behavior of tantalum and tantalum-tungsten alloys. Metall. Mater. Trans. A 27, 2994-3006.

Cho, H., Bronkhorst, C.A., Mourad, H.M., Mayeur, J.R., Luscher, D.J., 2018. Anomalous plasticity of body-centered-cubic crystals with non-Schmid effect. Int. J. Solids Struct. 139–140, 138–149.

Chowdhury, S.R., Roy, D., 2019. A non-equilibrium thermodynamic model for viscoplasticity and damage: Two temperatures and a generalized fluctuation relation. Int. J. Plast. 113, 158–184.

Christian, J.W., 1983. Some surprising features of the plastic deformation of body-centered cubic metals and alloys. Metall. Trans. A 14 (7), 1237–1256.

Cui, Y., Po, G., Srivastava, P., Jiang, K., Gupta, V., Ghoniem, N., 2020. The role of slow screw dislocations in controlling fast strain avalanche dynamics in body-centered cubic metals. Int. J. Plast. 124, 117–132.

Cuitiño, A.M., Ortiz, M., 1993. Computational modelling of single crystals. Modelling Simul. Mater. Sci. Eng. 1 (3), 225-263.

Danielsson, M., Parks, D.M., Boyce, M.C., 2002. Three-dimensional micromechanical modeling of voided polymeric materials. J. Mech. Phys. Solids 50 (2), 351-379.

Dequiedt, J.L., Denoual, C., Madec, R., 2015. Heterogeneous deformation in ductile FCC single crystals in biaxial stretching: the influence of slip system interactions. J. Mech. Phys. Solids 83, 301–318.

Devincre, B., Hoc, T., Kubin, L.P., 2005. Collinear interactions of dislocations and slip systems. Mater. Sci. Eng. A 400-401, 182-185.

El Ters, P., Shehadeh, M.A., 2019. Modeling the temperature and high strain rate sensitivity in BCC iron: Atomistically informed multiscale dislocation dynamics simulations. Int. J. Plast. 112, 257–277.

Follansbee, P.S., Kocks, U.F., 1988. A constitutive description of the deformation of copper based on the use of the mechanical threshold stress as an internal state variable. Acta Metall. 36 (1), 81–93.

Foster, R.C., Vander Wiel, S., Anghel, V., Bronkhorst, C., 2021. Towards random generation of microstructures of spatially varying materials from orthogonal sections. Comput. Mater. Sci. 192, 110313.

Francis, T., Rottmann, P.F., Polonsky, A.T., Charpagne, M.-A., Echlin, M.P., Anghel, V., Jones, D.R., Gray, G.T., De Graef, M., Pollock, T.M., 2021. Multimodal 3D characterization of voids in shock-loaded tantalum: Implications for ductile spallation mechanisms. Acta Mater. 215, 117057.

Gröger, R., 2021. Symmetry-adapted single crystal yield criterion for non-Schmid materials. Int. J. Plast. 146, 103101.

Gröger, R., Bailey, A.G., Vitek, V., 2008a. Multiscale modeling of plastic deformation of molybdenum and tungsten: I. Atomistic studies of the core structure and glide of 1/2<1 1 1> screw dislocations at 0 K. Acta Mater. 56 (19), 5401–5411.

Gröger, R., Racherla, V., Bassani, J.L., Vitek, V., 2008b. Multiscale modeling of plastic deformation of molybdenum and tungsten: II. Yield criterion for single crystals based on atomistic studies of glide of 1 / 2 < 111 > screw dislocations. Acta Mater. 56 (19), 5412–5425.

Gröger, R., Vitek, V., 2019. Impact of non-Schmid stress components present in the yield criterion for BCC metals on the activity of 110< 111 > slip systems. Comput. Mater. Sci. 159, 297–305.

Gröger, R., Vitek, V., 2020. Single crystal yield criterion for chromium based on atomistic studies of isolated 1/2[111] screw dislocations. Int. J. Plast. 132, 102733.

Hansen, B.L., Bronkhorst, C.A., Ortiz, M., 2010. Dislocation subgrain structures and modeling the plastic hardening of metallic single crystals. Modelling Simul. Mater. Sci. Eng. 18 (5), 055001.

Hochrainer, T., 2016. Thermodynamically consistent continuum dislocation dynamics. J. Mech. Phys. Solids 88, 12-22.

Holzer, J., Chlup, Z., Kruml, T., Gröger, R., 2021. Plastic deformation of magnetically isotropic Cr single crystals compressed at 77 K. Int. J. Plast. 138, 102938. Hull, D., Byron, J., Noble, F., 1967. Orientation dependence of yield in body-centered cubic metals. Can. J. Phys. 45 (2), 1091–1099.

Jafari, M., Jamshidian, M., Ziaei-Rad, S., 2017. A finite-deformation dislocation density-based crystal viscoplasticity constitutive model for calculating the stored deformation energy. Int. J. Mech. Sci. 128–129, 486–498.

Jiang, M., Devincre, B., Monnet, G., 2019. Effects of the grain size and shape on the flow stress: A dislocation dynamics study. Int. J. Plast. 113, 111-124.

- Kalidindi, S.R., Bronkhorst, C.A., Anand, L., 1992. Crystallographic texture evolution in bulk deformation processing of FCC metals. J. Mech. Phys. Solids 40 (3), 537-569.
- Knezevic, M., Beyerlein, I.J., Lovato, M.L., Tomé, C.N., Richards, A.W., McCabe, R.J., 2014. A strain-rate and temperature dependent constitutive model for BCC metals incorporating non-Schmid effects: Application to tantalum-tungsten alloys. Int. J. Plast. 62, 93–104.
- Kochmann, D.M., Hackl, K., 2011. The evolution of laminates in finite crystal plasticity: A variational approach. Contin. Mech. Thermodyn. 23 (1), 63-85.
- Kocks, U.F., Tomé, C.N., Wenk, H.-R., 1998. Texture and Anisotropy: Preferred Orientations in Polycrystals and their Effect on Materials Properties. Cambridge University Press.
- Kothari, M., Anand, L., 1998. Elasto-viscoplastic constitutive equations for polycrystalline metals: Application to tantalum. J. Mech. Phys. Solids 46 (1), 51-83.
- Langer, J.S., 2015. Statistical thermodynamics of strain hardening in polycrystalline solids. Phys. Rev. E 92 (3), 032125.
- Langer, J.S., Bouchbinder, E., Lookman, T., 2010. Thermodynamic theory of dislocation-mediated plasticity. Acta Mater. 58 (10), 3718-3732.
- Le, K.C., 2018. Thermodynamic dislocation theory for non-uniform plastic deformations. J. Mech. Phys. Solids 111, 157-169.
- Le, K.C., 2019. Thermodynamic dislocation theory: Finite deformations. Internat. J. Engrg. Sci. 139, 1-10.
- Le, K.C., Dang, S.L., Luu, H.T., Gunkelmann, N., 2021. Thermodynamic dislocation theory: application to BCC-crystals. Modelling Simul. Mater. Sci. Eng. 29 (1), 015003.
- Levitas, V.I., Javanbakht, M., 2015. Thermodynamically consistent phase field approach to dislocation evolution at small and large strains. J. Mech. Phys. Solids 82, 345–366.
- Lieberman, E.J., Lebensohn, R.A., Menasche, D.B., Bronkhorst, C.A., Rollett, A.D., 2016. Microstructural effects on damage evolution in shocked copper polycrystals. Acta Mater. 116, 270–280.
- Lieou, C.K., Bronkhorst, C.A., 2020. Thermodynamic theory of crystal plasticity: formulation and application to polycrystal FCC copper. J. Mech. Phys. Solids 138, 103905
- Lieou, C.K., Bronkhorst, C.A., 2021. Thermomechanical conversion in metals: dislocation plasticity model evaluation of the Taylor-Quinney coefficient. Acta Mater. 202. 170–180.
- Lim, H., Battaile, C.C., Brown, J.L., Weinberger, C.R., 2016. Physically-based strength model of tantalum incorporating effects of temperature, strain rate and pressure. Modelling Simul. Mater. Sci. Eng. 24 (5), 055018.
- Lim, H., Battaile, C.C., Carroll, J.D., Boyce, B.L., Weinberger, C.R., 2015. A physically based model of temperature and strain rate dependent yield in BCC metals: Implementation into crystal plasticity. J. Mech. Phys. Solids 74, 80–96.
- Lim, H., Carroll, J.D., Battaile, C.C., Buchheit, T.E., Boyce, B.L., Weinberger, C.R., 2014. Grain-scale experimental validation of crystal plasticity finite element simulations of tantalum oligocrystals. Int. J. Plast. 60, 1–18.
- Lim, H., Carroll, J.D., Michael, J.R., Battaile, C.C., Chen, S.R., D. Lane, J.M., 2020. Investigating active slip planes in tantalum under compressive load: Crystal plasticity and slip trace analyses of single crystals. Acta Mater. 185, 1–12.
- Lim, H., Jong Bong, H., Chen, S.R., Rodgers, T.M., Battaile, C.C., Lane, J.M.D., 2018. Developing anisotropic yield models of polycrystalline tantalum using crystal plasticity finite element simulations. Mater. Sci. Eng. A 730, 50–56.
- Lim, H., Noell, P.J., Carroll, J.D., 2021. Crystallographic orientation dependent fracture behavior in tantalum single crystals. Scr. Mater. 191, 76-80.
- Losko, A.S., Vogel, S.C., Reiche, H.M., Nakotte, H., 2014. A six-axis robotic sample changer for high-throughput neutron powder diffraction and texture measurements. J. Appl. Crystallogr. 47 (6), 2109–2112.
- Ma, A., Roters, F., 2004. A constitutive model for fcc single crystals based on dislocation densities and its application to uniaxial compression of aluminium single crystals. Acta Mater. 52 (12), 3603–3612.
- Ma, A., Roters, F., Raabe, D., 2007. A dislocation density based constitutive law for BCC materials in crystal plasticity FEM. Comput. Mater. Sci. 39 (1), 91–95. Madec, R., Devincre, B., Kubin, L., Hoc, T., Rodney, D., 2003. The role of collinear interaction in dislocation-induced hardening. Science 301 (5641), 1879–1882. Madec, R., Kubin, L.P., 2017. Dislocation strengthening in FCC metals and in BCC metals at high temperatures. Acta Mater. 126, 166–173.
- Matsuno, H., Yokoyama, A., Watari, F., Uo, M., Kawasaki, T., 2001. Biocompatibility and osteogenesis of refractory metal implants, titanium, hafnium, niobium, tantalum and rhenium. Biomaterials 22 (11), 1253–1262.
- Matthies, S., Pehl, J., Wenk, H.R., Lutterotti, L., Vogel, S.C., 2005. Quantitative texture analysis with the HIPPO neutron TOF diffractometer. J. Appl. Crystallogr. 38 (3), 462–475.
- Mayeur, J.R., Beyerlein, I.J., Bronkhorst, C.A., Mourad, H.M., Hansen, B.L., 2013. A crystal plasticity study of heterophase interface character stability of Cu/Nb bicrystals. Int. J. Plast. 48, 72–91.
- Millett, J.C.F., Avraam, P., Whiteman, G., Chapman, D.J., Case, S., 2020. The role of orientation on the shock response of single crystal tantalum. J. Appl. Phys. 128 (3), 035104.
- Narayanan, S., McDowell, D.L., Zhu, T., 2014. Crystal plasticity model for BCC iron atomistically informed by kinetics of correlated kinkpair nucleation on screw dislocation. J. Mech. Phys. Solids 65, 54–68.
- Nemat-Nasser, S., Okinaka, T., Ni, L., 1998. A physically-based constitutive model for BCC crystals with application to polycrystalline tantalum. J. Mech. Phys. Solids 46 (6), 1009–1038.
- Nguyen, T., Fensin, S.J., Luscher, D.J., 2021. Dynamic crystal plasticity modeling of single crystal tantalum and validation using Taylor cylinder impact tests. Int. J. Plast. 139, 102940.
- Nieto-Fuentes, J.C., Rittel, D., Osovski, S., 2018. On a dislocation-based constitutive model and dynamic thermomechanical considerations. Int. J. Plast. 108,
- Noell, P., Carroll, J., Hattar, K., Clark, B., Boyce, B., 2017. Do voids nucleate at grain boundaries during ductile rupture? Acta Mater. 137, 103-114.
- Ortiz, M., Repetto, E.A., 1999. Nonconvex energy minimization and dislocation structures in ductile single crystals. J. Mech. Phys. Solids 47 (2), 397-462.
- Ortiz, M., Repetto, E., Stainier, L., 2000. A theory of subgrain dislocation structures. J. Mech. Phys. Solids 48 (10), 2077-2114.
- Ortiz, M., Stainier, L., 1999. The variational formulation of viscoplastic constitutive updates. Comput. Methods Appl. Mech. Engrg. 171 (3-4), 419-444.
- Pappu, S., Kennedy, C., Murr, L.E., Meyers, M.A., 1996. Deformation twins in a shock-loaded Ta-2.5w/oW precursor plate and a recovered, Ta-2.5w/oW explosively formed penetrator. Scr. Mater. 35 (8), 959–965.
- Petryk, H., 2020. A quasi-extremal energy principle for non-potential problems in rate-independent plasticity. J. Mech. Phys. Solids 136, 103691.
- Petryk, H., Kursa, M., 2013. The energy criterion for deformation banding in ductile single crystals. J. Mech. Phys. Solids 61 (8), 1854-1875.
- Petryk, H., Kursa, M., 2022. Crystal plasticity algorithm based on the quasi-extremal energy principle. Internat. J. Numer. Methods Engrg. 123 (14), 3285-3316.
- Po, G., Huang, Y., Ghoniem, N., 2019. A continuum dislocation-based model of wedge microindentation of single crystals. Int. J. Plast. 114, 72–86.
- Pokharel, R., Lind, J., Kanjarla, A.K., Lebensohn, R.A., Li, S.F., Kenesei, P., Suter, R.M., Rollett, A.D., 2014. Polycrystal plasticity: Comparison between grain Scale observations of deformation and simulations. Ann. Rev. Condens. Matter Phys. 5 (1), 317–346.
- Quey, R., Dawson, P.R., Barbe, F., 2011. Large-scale 3D random polycrystals for the finite element method: Generation, meshing and remeshing. Comput. Methods Appl. Mech. Engrg. 200 (17–20), 1729–1745.
- Queyreau, S., Monnet, G., Devincre, B., 2009. Slip systems interactions in α-iron determined by dislocation dynamics simulations. Int. J. Plast. 25 (2), 361–377. Ribárik, G., Gubicza, J., Ungár, T., 2004. Correlation between strength and microstructure of ball-milled Al-Mg alloys determined by X-ray diffraction. Mater. Sci. Eng. A 387–389, 343–347.
- Rietveld, H.M., 1969. A profile refinement method for nuclear and magnetic structures. J. Appl. Crystallogr. 2 (2), 65-71.

Rittel, D., Silva, M.L., Poon, B., Ravichandran, G., 2009. Thermomechanical behavior of single crystalline tantalum in the static and dynamic regime. Mech. Mater. 41 (12), 1323–1329.

Rittel, D., Zhang, L., Osovski, S., 2017. The dependence of the Taylor–Quinney coefficient on the dynamic loading mode. J. Mech. Phys. Solids 107, 96–114. Rivera-Díaz-del-Castillo, P.E.J., Huang, M., 2012. Dislocation annihilation in plastic deformation: I. Multiscale irreversible thermodynamics. Acta Mater. 60 (6–7), 2606–2614.

Roy, A., Acharya, A., 2005. Finite element approximation of field dislocation mechanics. J. Mech. Phys. Solids 53 (1), 143-170.

Roy, A., Acharya, A., 2006. Size effects and idealized dislocation microstructure at small scales: Predictions of a Phenomenological model of Mesoscopic Field Dislocation Mechanics: Part II. J. Mech. Phys. Solids 54 (8), 1711–1743.

Savage, D.J., Beyerlein, I.J., Knezevic, M., 2017. Coupled texture and non-Schmid effects on yield surfaces of body-centered cubic polycrystals predicted by a crystal plasticity finite element approach. Int. J. Solids Struct. 109, 22–32.

Savage, D.J., Chandola, N., Cazacu, O., McWilliams, B.A., Knezevic, M., 2018. Validation of recent analytical dilatational models for porous polycrystals using crystal plasticity finite element models with Schmid and non-Schmid activation laws. Mech. Mater. 126, 148–162.

Seeger, A., 1995. The flow stress of high-purity refractory body-centred cubic metals and its modification by atomic defects. Le J. Physique IV 05 (C7), C7–45–C7–65.

Seeger, A., 2001. Why anomalous slip in body-centred cubic metals? Mater. Sci. Eng. A 319-321, 254-260.

Sherwood, P.J., Guiu, F., Kim, H.C., Pratt, P.L., 1967. Plastic anisotropy of tantalum, niobium, and molybdenum. Can. J. Phys. 45 (2), 1075-1089.

Shizawa, K., Kikuchi, K., Zbib, H.M., 2001. A strain-gradient thermodynamic theory of plasticity based on dislocation density and incompatibility tensors. Mater. Sci. Eng. A 309–310, 416–419.

Stainier, L., Cuitiño, A.M., Ortiz, M., 2002. A micromechanical model of hardening, rate sensitivity and thermal softening in BCC single crystals. J. Mech. Phys. Solids 50 (7), 1511–1545.

Takajo, S., Vogel, S.C., 2018. Determination of pole figure coverage for texture measurements with neutron time-of-flight diffractometers. J. Appl. Crystallogr. 51 (3), 895–900.

Taylor, G.I., Quinney, H., 1934. The latent energy remaining in a metal after cold working. Proc. R. Soc. Lond. Ser. A 143 (849), 307-326.

Vidyasagar, A., Tutcuoglu, A.D., Kochmann, D.M., 2018. Deformation patterning in finite-strain crystal plasticity by spectral homogenization with application to magnesium. Comput. Methods Appl. Mech. Engrg. 335, 584–609.

Vogel, S.C., Hartig, C., Lutterotti, L., Von Dreele, R.B., Wenk, H.-R., Williams, D.J., 2004. Texture measurements using the new neutron diffractometer HIPPO and their analysis using the Rietveld method. Powder Diffr. 19 (1), 65–68.

Weinberger, C.R., Boyce, B.L., Battaile, C.C., 2013. Slip planes in bcc transition metals. Int. Mater. Rev. 58 (5), 296-314.

Wenk, H.R., Lutterotti, L., Vogel, S., 2003. Texture analysis with the new HIPPO TOF diffractometer. Nucl. Instrum. Methods Phys. Res. Sect. A 515 (3), 575–588. Wenk, H.-R., Lutterotti, L., Vogel, S.C., 2010. Rietveld texture analysis from TOF neutron diffraction data. Powder Diffr. 25 (3), 283–296.

Weygand, D., Mrovec, M., Hochrainer, T., Gumbsch, P., 2015. Multiscale simulation of plasticity in BCC metals. Ann. Rev. Mater. Res. 45, 369-390.

Whiteman, G., Case, S., Millett, J.C.F., Cox, M.J., Avraam, P., Dear, J.P., Sancho, A., Hooper, P.A., 2019. Uniaxial compression of single crystal and polycrystalline tantalum. Mater. Sci. Eng. A 759, 70–77.

Yalçınkaya, T., Brekelmans, W.A.M., Geers, M.G.D., 2012. Non-convex rate dependent strain gradient crystal plasticity and deformation patterning. Int. J. Solids Struct. 49 (18), 2625–2636.

Zecevic, M., Knezevic, M., 2018. A new visco-plastic self-consistent formulation implicit in dislocation-based hardening within implicit finite elements: Application to high strain rate and impact deformation of tantalum. Comput. Methods Appl. Mech. Engrg. 341, 888–916.

Zerilli, F.J., Armstrong, R.W., 1987. Dislocation-mechanics-based constitutive relations for material dynamics calculations. J. Appl. Phys. 61 (5), 1816–1825.